GEOLOGICA CARPATHICA, 2025, 76, 3, 171–188 https://doi.org/10.31577/GeolCarp.2025.07

Allanite to monazite transition and dating of prograde Eo-Alpine metamorphism in the Veporic Unit, Western Carpathians (Slovakia)

MARIAN JANÁK[1,✉], IGOR PETRÍK[1], DUŠAN PLAŠIENKA[2], NIKOLAUS FROITZHEIM[3] and PATRIK KONEČNÝ[4]

[1]Earth Science Institute, Slovak Academy of Sciences, 840 05 Bratislava, Slovakia
[2]Department of Geology and Paleontology, Comenius University, 842 15 Bratislava, Slovakia
[3]Steinman Institute of Geology, Mineralogy and Paleontology, University of Bonn, Germany
[4]Dionýz Štúr State Geological Institute, 817 04 Bratislava, Slovakia

(Manuscript received April 2, 2025; accepted in revised form July 2, 2025; Associate Editor: Pavel Uher)

Abstract: Monazite and allanite are important tools for dating prograde and peak metamorphism. Rising temperature together with suitable bulk-rock composition results in allanite replacement by monazite. To constrain the timing of prograde Eo-Alpine metamorphism in the Veporic Unit of the Western Carpathians we dated monazite using electron microprobe. The dated monazite occurs in garnet mica schists exposed from the deepest levels of the Veporic dome. The peak metamorphic assemblage consists of garnet + biotite + phengite + paragonite + rutile + quartz. Alpine garnet is zoned with decreasing Ca and increasing Mg from the core to the rim reflecting prograde growth. Monazite-(Ce) occurs in the chlorite, muscovite and biotite matrix occasionally associated with allanite-(Ce)–(REE-epidote/clinozoisite) and xenotime-(Y), suggesting monazite formation via allanite breakdown. Formation of monazite was controlled by rising temperature and low-Ca bulk-rock composition; the monazite-rich sample shows a CaO/Na_2O ratio of 0.47. Dating of monazite yielded Cretaceous weighted average Th–U–total Pb age of 95.8±2.7 Ma (MSWD = 1.13) with individual dates ranging from 75 to 124 Ma. Thermodynamic modelling suggests allanite–monazite transition along a prograde *P–T* path, from the stability field of allanite (6–8 kbar; 520–540 °C) approximated by epidote-zoisite, to peak conditions (12–14 kbar; 580–600 °C) constrained by the composition of garnet, phengitic muscovite and biotite, and Zr-in rutile thermometry. The age of 96 Ma refers, therefore, to the prograde metamorphic stage, close to peak *P–T* conditions, which is in excellent agreement with the timing of Eo-Alpine HP/UHP metamorphism (100–90 Ma) in the Austroalpine Nappes. This supports the correlation of Eo-Alpine metamorphism in the Western Carpathians with intracontinental subduction in the Eastern Alps.

Keywords: allanite–monazite transition, prograde metamorphism, monazite dating, Eo-Alpine metamorphism, Western Carpathians

Introduction

Monazite and allanite, the most important carriers of light rare elements (LREE) in felsic metamorphic rocks, are increasingly used for dating prograde and peak metamorphic conditions (e.g., Smith & Barreiro 1990; Janots et al. 2009; Gregory et al. 2012; Skrzypek et al. 2017; Stumpf et al. 2024). Crossing the allanite/dissakisite stability window by rising temperature results in allanite replacement by monazite (Smith & Barreiro 1990; Wing et al. 2003; Janots et al. 2008). Consequently, both allanite and monazite can precisely date prograde metamorphic evolution in combination with calculated *P–T* conditions.The upper stability boundary of allanite strongly depends on bulk Ca and Al content; the higher the Ca content in the system (whole rock) is, the higher is the temperature necessary for transformation of allanite to monazite (Janots et al. 2008; Spear 2010). Allanite cores may commonly preserve older ages from earlier metamorphic or magmatic events.

The Western Carpathians (WeCa) form the northernmost arc of the European Alpides connected with the Eastern Alps to the West and Eastern Carpathians to the East. The Central Western Carpathians represent a tectonic system that can be well correlated with the Austroalpine units of the Alps. Eo-Alpine metamorphism, related to the Cretaceous orogenic events, has been recognised in the Veporic Unit (e.g., Vrána 1964; Vozárová 1990; Méres & Hovorka 1991; Plašienka et al. 1999; Lupták et al. 2000, 2003; Janák et al. 2001; Jeřábek et al. 2008). Increasing *P–T* conditions from greenschist to middle amphibolite facies reflect a coherent metamorphic field gradient in the deeply buried Veporic complexes. Exhumation during the Late Cretaceous has been dated by various cooling ages (e.g., Maluski et al. 1993; Dallmeyer et al. 1996; Janák et al. 2001; Putiš et al. 2009; Vojtko et al. 2016). However, there is a shortage of geochronological data on prograde metamorphism (e.g., Bukovská et al. 2013).

✉ corresponding author: Marian Janák
marian.janak@savba.sk

In this paper, we used monazite to date prograde Eo-Alpine metamorphism in the Veporic Unit. Two representative samples of garnet mica schist were selected, both samples shared similar *P–T* evolution but formation of monazite from allanite was controlled by bulk-rock composition. Monazite was dated *in situ* from thin sections using electron microprobe. The *P–T* conditions of metamorphism were constrained by thermodynamic modelling, and correlation aspects with the Austroalpine units of the Eastern Alps are discussed.

Geological setting

The general regional division of the Western Carpathians is based on the presence of oceanic suture zones and/or fossil plate boundaries. Accordingly, a threefold division of the Western Carpathians has been used (e.g., Froitzheim et al. 2008; Plašienka 2018). The External Western Carpathians (EWC) and Central Western Carpathians (CWC) are separated by the Pieniny Klippen Belt (Fig. 1) as a surface expression of the Late Cretaceous to Eocene closing of the Penninic (Alpine Atlantic) oceanic domains (e.g., Plašienka et al. 2020 and references therein). The Early Alpine Meliata suture separates the IWC (Internal Western Carpathians) from the CWC. The Meliata suture zone originated during the Late Jurassic after closure of the Neotethys-related Meliata Ocean (e.g., Kozur 1991; Dallmeyer et al. 2008; Plašienka et al. 2019). Its regional course is largely hidden beneath Cenozoic complexes; supposedly it follows the large-scale pre-Miocene Rába and Hurbanovo–Diósjenő fault zones (Fig. 1). under Neogene sediments of the Pannonian Basin system according to Plašienka & Bielik (2024). The Cretaceous CWC nappe stack consists of three thick-skinned thrust sheets (Tatric, Veporic and Gemeric from bottom to top) that are overridden by three décollement nappe systems (Fatric, Hronic and Silicic). The Tatric and Veporic superunits include predominantly high-grade and the Gemeric sheet low-grade pre-Alpine volcano-sedimentary basement complexes intruded by Variscan granitoid bodies. Their post-Variscan sedimentary cover is composed of the Upper Paleozoic and Mesozoic formations.

The Veporic superunit represents the metamorphic core of the WeCa orogen. Its deepest exposed parts underwent Eo-Alpine (Cretaceous) metamorphism under amphibolite-facies conditions (Janák et al. 2001; Jeřábek et al. 2008). It forms a crustal-scale thrust wedge that overlies the Tatric sheet and is overridden by the Gemeric and higher units. The pre-Alpine crystalline basement of the Veporic Unit is composed of polymetamorphic (Variscan and Alpine) metasediments and subordinate metavolcanics intruded by the Variscan granitoid pluton (Kráľova hoľa complex). Polymetamorphic evolution of the Veporic Unit with Variscan metamorphism reaching amphibolite facies conditions is well known (e.g., Jeřábek et al. 2008, 2012). The Veporic belt is subdivided into several subparallel, SW–NE trending zones separated by regional fault zones.

The investigated southern Veporic area embraces the Kráľova hoľa and Kohút zones (Fig. 2), which are separated by the Cenozoic Muráň fault (Gerátová et al. 2022). The basement and cover complexes of the southernmost Veporic Kohút Zone are overthrust by the Gemeric basement sheet along

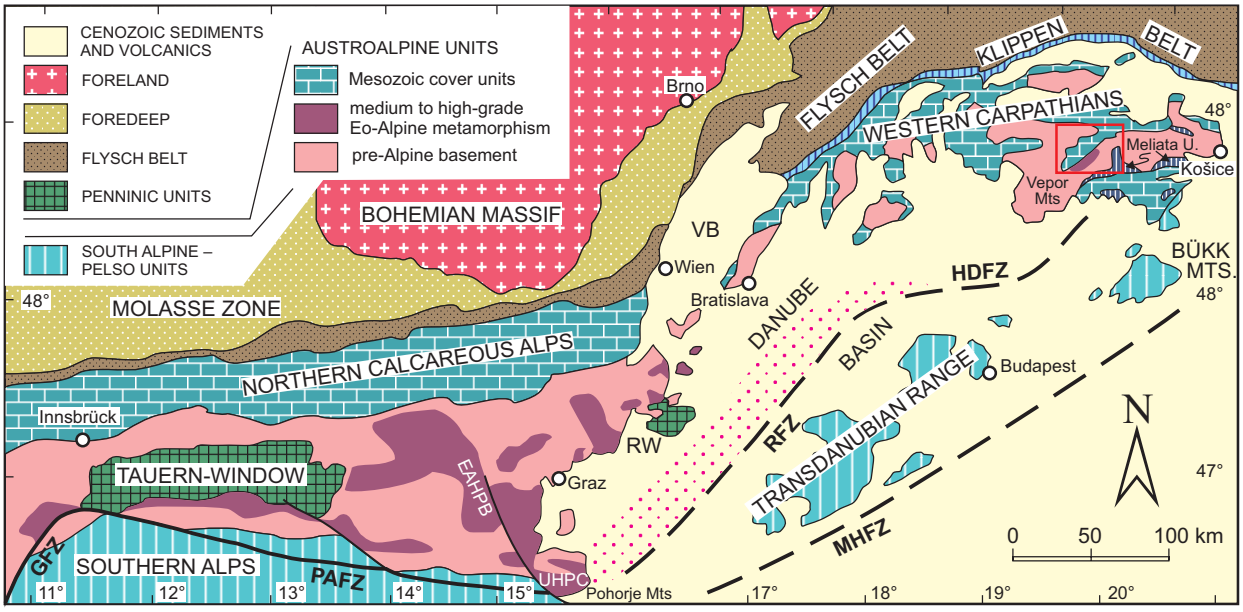

Fig. 1. Sketch map of principal tectonic units of the Eastern Alps and Western Carpathians and their foreland (modified after Janák et al. 2001 and Plašienka & Bielik 2024). Abbreviations: GFZ – Giudicarie fault zone; PAFZ – Peri-Adriatic fault zone; RW – Rechnitz window; VB – Vienna basin; RFZ – Rába fault zone; HDFZ – Hurbanovo–Diósjenő fault zone; MHFZ – Mid-Hungarian fault zone. Red rectangle shows area shown in Figure 2, red-dotted zone north-west of RFZ indicates a possible continuation of the Eo-Alpine high-pressure belt (EAHPB) in the basement under Neogene sediments of the Pannonian Basin system according to Plašienka & Bielik (2024).

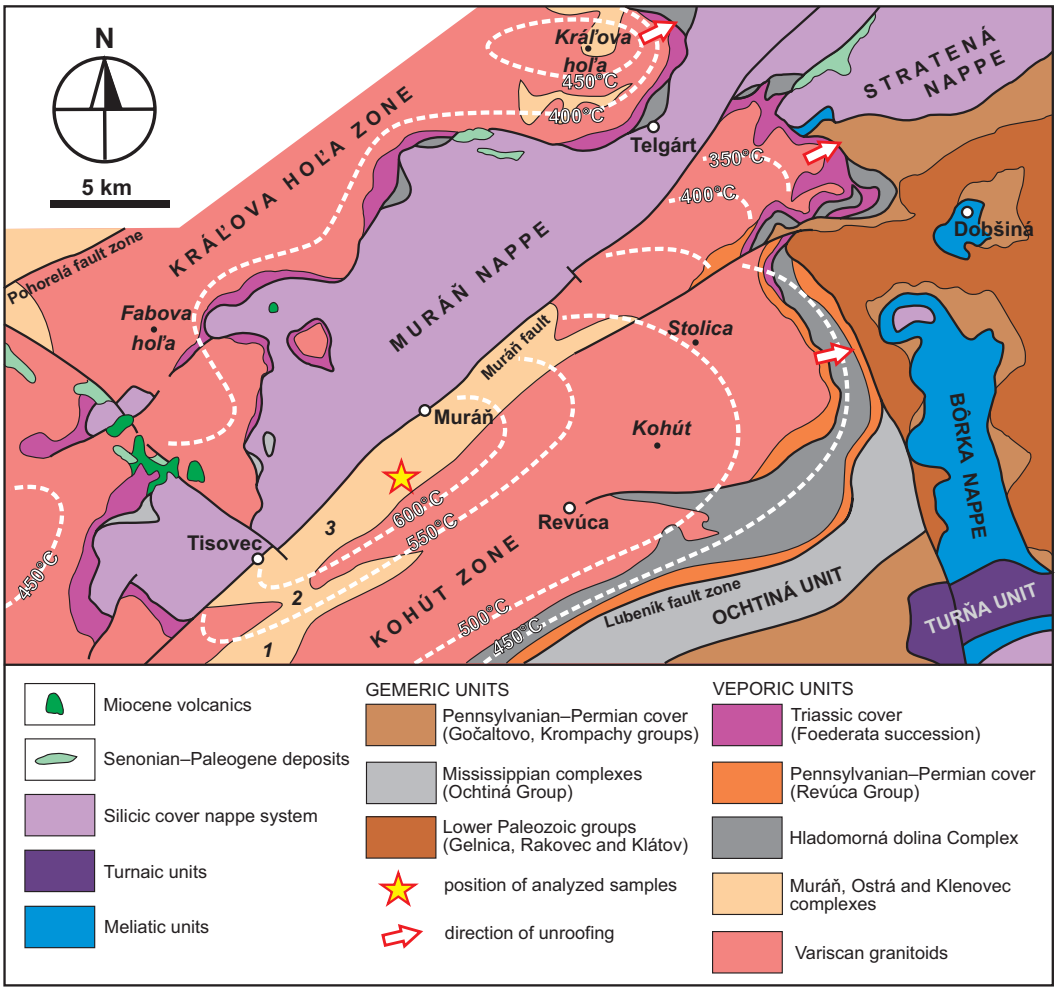

Fig. 2. Geological map of the eastern part of the Veporic and overlying units in central Slovakia. Eo-Alpine metamorphic zones and isotherms according to Janák et al. (2001) and Jeřábek et al. (2008). 1 – chloritoid+chlorite+garnet zone, 2 – garnet+staurolite+chlorite zone, 3 – staurolite+biotite+kyanite zone.

the Lubeník fault zone. The south Veporic basement is represented by several granitoid suites of the Vepor plutonic complex that intruded into metamorphosed sediments and basic volcanics differentiated into several complexes. These complexes were affected by Eo-Alpine metamorphism (Vrána 1964, 1966, 1980; Vozárová 1990; Méres & Hovorka 1991; Putiš 1991; Plašienka et al. 1999; Lupták et al. 2000; Janák et al. 2001; Jeřábek et al. 2008). The northwestern part of the Kohút Zone is built up by Ordovician felsic orthogneisses (Muráň Complex; Gaab et al. 2006), garnet mica schists (Ostrá Complex; e.g., Méres & Hovorka 1991; Janák et al. 2001), migmatitic paragneisses (Klenovec Complex) and the lithologically variable Sinec Complex. The southernmost part of the Kohút Zone is composed of the greenschist-facies Hladomorná dolina Complex (Klinec 1966, 1971; Fig. 2). The intrusive contact between the Variscan granitoids and metasediments of Hladomorná dolina Complex is disturbed by a zone of shear deformation related to the activity of the Lubeník fault zone. The hidden Upper Cretaceous granitic intrusion (Rochovce granite; Vozárová 1990; Poller et al. 2001; Kohút et al. 2013) drilled bellow the Hladomorná dolina Complex (Klinec 1980) affected the overlying complexes by contact metamorphism (Korikovsky et al. 1986). Along the southern Veporic–Gemeric contact zone, the Veporic cover complexes are represented by Pennsylvanian and Permian clastic deposits (Revúca Group; Vozárová & Vozár 1988; Vozárová 1996) and Lower Triassic quartzites unconformably overlying the Hladomorná dolina Complex (Fig. 2). In the central and eastern parts of the Kráľova hoľa and Kohút zones, the Variscan basement complexes are covered by Permian–Lower Triassic clastics and variable Middle–Upper Triassic platform and basinal carbonates (Foederata succession; e.g., Biely 1956; Plašienka 1993). Part of the Hladomorná dolina Complex, together with its sedimentary cover, was detached to form a thin-skinned Markuška Nappe (Plašienka 1980, 1984) that overlies the Foederata Mesozoic complexes along the eastern Veporic margin (Fig. 2). A similar position is occupied by the nappe outliers, or extensional allochthons, of

the Gemeric Ochtiná Unit occurring in the central Veporic parts below the Silicic Muráň Nappe (Plašienka & Soták 2001). The analysed samples belong to the Ostrá Complex in the northwestern part of the Kohút Zone.

Analytical methods

Electron microprobe WDS analysis of mineral chemistry was performed with a JEOL JXA 8530F instrument at the Earth Science Institute, Slovak Academy of Sciences in Banská Bystrica. The operating conditions for analysing silicates and oxides were as follows: 15 kV accelerating voltage, 20 nA beam current, counting times 10–20 s on peaks and beam diameter of 2–7 μm. Zirconium concentrations in rutile were measured using an accelerating voltage of 15 kV, probe current of 150 nA, a beam diameter of 3–7 μm depending on size of rutile, and accumulation times 300 sec on peak and 150 s on background. High-sensitive H- and L-type spectrometers were chosen for measuring zirconium. The following minerals and pure element oxides were used as standards for calibration: albite, diopside (Si Kα, Al Kα, Na Kα); orthoclase (K Kα); rhodonite (Mn Kα); hematite and almandine (Fe Kα); gahnite (Zn Kα, Ba Lα, S Kα); celestine (Sr Lα); rutile (Ti Kα); fluorite (F Kα); tugtupite (Cl Kα); Cr_2O_3 (Cr Kα); $ScVO_4$ (V Kα); apatite (P Kα); zircon (Zr Lα). The calculation of oxide wt% was made using the ZAF correction procedure.

Monazite dating was performed chemically by the MARC (monazite age reference correction) dating method developed in the Dionýz Štúr State Geological Institute in Bratislava (Konečný et al. 2018), using electron microprobe analyses from the CAMECA SX 100. Monazite spot analyses were acquired under 15 kV accelerating voltage, 180 nA beam current, and a 3 μm beam diameter to increase both counting efficiency and spatial resolution. Long counting times were used to increase the analytical precision: for Pb (300 s peak and 2×150 s backgrounds), Th (35 s peak and 2×17.5 s background), U (80 s peak and 80 s background), and Y (40 s peak and 2×20 s background). A set of 10 reference standards was utilized for assessment of minor systematic errors that cannot be suppressed in the currently used measuring procedure, but are accumulated regardless of the number of analyses. Other details and principles of MARC dating technique can be found in Konečný et al. (2018).

Results

Petrography and mineral chemistry

The investigated samples (V-9, VV-4) are garnet mica schists from the staurolite+biotite+kyanite zone, i.e. the highest-grade Eo-Alpine metamorphic zone in the southern Veporic unit (Fig. 2). The texture is affected by ductile deformation and folding (Fig. 3a). Garnet forms porphyroblasts in a schistose matrix composed of white mica (muscovite, paragonite) and biotite (Fig. 3b, c). The mineral assemblage ascribed to the Alpine metamorphism in both samples includes garnet, white mica (muscovite and paragonite), biotite, chlorite, plagioclase, quartz and rare tourmaline. In addition, sample V-9 contains minor staurolite in the matrix (Fig. 3c). In both samples, chlorite is considered to be primary with exception of minor retrograde flakes in sample VV-4. The peak metamorphic assemblage is garnet+biotite+phengite+paragonite +rutile+quartz. Staurolite and plagioclase are inferred to be formed as a result of paragonite–phengite–garnet breakdown during decompression from the peak metamorphic stage. Accessory minerals are rutile, ilmenite, zircon, allanite (REE-epidote) and monazite.

In both samples iIlmenite and rutile occur in the matrix and as inclusions in garnet. In sample V-9 inclusions of pure ilmenite are in the garnet cores (Fig. 3e) whereas those of rutile are in the garnet rims (Fig. 3d). Matrix ilmenite is often rimmed by rutile or rutile is partly replaced by ilmenite. In sample VV-4, rutile is mostly replaced by ilmenite.

Garnet occurs in both samples as clusters involving fragments of fractured (possibly pre-Alpine) garnet and newly-formed, idioblastic Alpine garnet. Alpine garnet contains inclusions of quartz, ilmenite and allanite (REE-epidote) in the cores and rutile in the rims (Fig. 3e, f). Garnet belongs to almandine dominant member (69 to 75 mol%) with 12 to 23 mol% grossular, 5 to 12 mol% pyrope and 1 to 3 mol% spessartine (Table 1). Compositional maps and profiles of Alpine garnet (Fig. 4) show that it is zoned with the almandine and pyrope components increasing, and spessartine, grossular and Fe/(Fe+Mg) ratio decreasing from core to rim. Garnet displays an oscillatory zoning with Ca enrichment and Fe depletion in the rim (Figs. 4, 5). A more detailed profile of garnet (sample VV-4, Fig. 5) shows Ca annulus at the boundary with allanite inclusions. In the outer rim almandine decreases while spessartine slightly increases. This suggests a prograde growth evolution and minor retrogression of garnet during a single metamorphic event. Representative analyses of garnet are in Table 1. *White mica* compositions range from phengite (up to Si=3.21 apfu) to muscovite and paragonite (Table 2). *Biotite* shows annite to phlogopite composition with Mg/(Mg+Fe) ratio=0.5–0.6, TiO_2 content varies from 1.5 to 1.6 wt% (Table 2). *Plagioclase* compositions range from An_{17} to An_{20}. *Staurolite* is Fe-rich with Fe/(Fe+Mg) ratio=0.8, and 2.5 wt% ZnO.

Allanite–monazite petrographic observations

Allanite is found both in the matrix and enclosed within garnets (Fig. 6a, b, e). Grain clusters up to 300 μm in length occur among muscovite flakes accompanied by quartz, rutile and biotite. Small (20–40 μm across) subhedral crystals of both allanite and REE-epidote are enclosed within garnet (Fig. 6c,d). In the sample with increased calcium content (V-9) *apatite* forms clusters (250–500 μm across) and encloses small allanites (Fig. 6f). The clusters may contain monazite

and Th-silicate crystals arranged around their border. Both matrix and enclosed allanites show sector zoning (Fig. 6d).

Monazite is commonly found in the mica-rich matrix. Subhedral crystals (between 10 and 50 μm) occur associated with matrix allanite, zircon and xenotime (Fig. 6g, h), or with ilmenite and zircon. Monazite also occurs independently within muscovite, paragonite and chlorite layers. The size of subhedral monazite crystals is between 10 and 50 μm. No monazite was found enclosed in garnet.

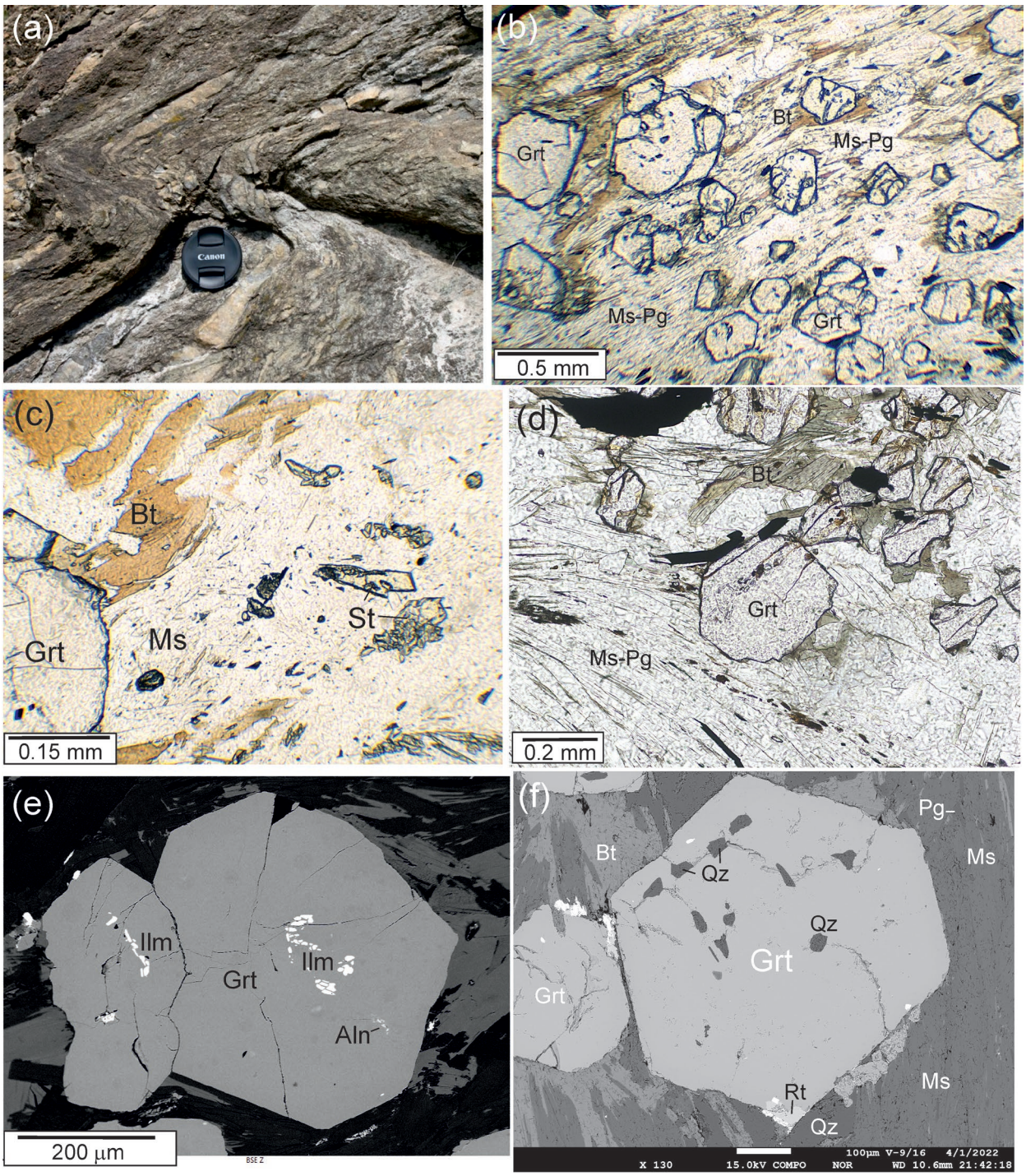

Fig. 3. **a** — Macrophotograph of garnet mica schist from the southern Veporic unit. The texture is affected by ductile folding. **b, c** — Microphotographs of garnet mica schist (sample V-9) with garnet (Grt) porphyroblasts in the matrix composed of muscovite–paragonite (Ms-Pg) and biotite (Bt), with minor staurolite (St). **d** — Microphotograph of sample VV-4 with garnet porphyroblasts in the matrix composed of muscovite–paragonite and biotite. **e, f** — Back scattered electron (BSE) images of garnet with inclusions of quartz (Qz) rutile (Rt), ilmenite (Ilm) and allanite (Aln) in sample VV-4.

Table 1: Representative analyses of garnet.

	V-9 Grt core	V-9 Grt rim	V-9 Grt core	V-9 Grt rim	VV-4 Grt core	VV-4 Grt rim	VV-4 Grt core	VV-4 Grt rim
SiO_2	36.58	36.6	36.61	37.22	37.19	37.5	37.27	37.66
TiO_2	0.02	0.02	0.09	0.07	0.07	0.03	0.05	0.05
Al_2O_3	21.13	21.32	21.18	21.46	21.13	21.37	21.07	21.35
FeOt	31.26	31.64	30.92	31.96	32.56	33.47	32.47	33.45
MnO	1.45	0.89	1.08	1.01	0.5	0.93	0.62	0.75
MgO	1.18	3	1.23	2.63	2.11	3.04	2.11	2.96
CaO	8.07	5.57	7.86	5.43	6.72	4.07	5.86	4.21
Total	99.69	99.04	98.97	99.78	100.28	100.41	99.45	100.43
Calculated to 12 oxygens								
Si	2.959	2.964	2.972	2.981	2.978	2.99	3.002	2.999
Ti	0.001	0.001	0.005	0.004	0.004	0.002	0.003	0.003
Al	2.015	2.023	2.027	2.026	1.995	2.009	2.001	2.004
Fe	2.115	2.13	2.099	2.141	2.181	2.232	2.187	2.228
Mn	0.099	0.099	0.074	0.069	0.034	0.063	0.042	0.051
Mg	0.142	0.36	0.149	0.314	0.252	0.361	0.253	0.351
Ca	0.7	0.48	0.684	0.466	0.577	0.348	0.506	0.359
Total	8.031	8.057	8.01	8.001	8.021	8.005	7.994	7.995
XPrp	0.05	0.12	0.05	0.11	0.08	0.12	0.08	0.12
XGrs	0.23	0.16	0.23	0.16	0.19	0.12	0.17	0.12
XAlm	0.69	0.69	0.70	0.72	0.72	0.74	0.73	0.75
XSps	0.03	0.03	0.02	0.02	0.01	0.02	0.01	0.02

Compositions of allanite and monazite

Allanite compositions (samples VV-4, V-9; Table 3) are illustrated in Fig. 7. The compositions from both samples spread between allanite, epidote and clinozoisite on the Al-rich side of the plot (after Petrík et al. 1995), allanite in sample V-9 being more aluminous than VV-4. Three points with low REE correspond to REE-rich epidote/clinozoisite, all included in garnet (Fig. 6). Allanite has low Th and U contents, around 0.2 wt% ThO_2, and below 0.15 wt% U. Two analyses of a grain enclosed by biotite have 1.8 wt% ThO_2 and 0.25 wt% UO_2.

Almost 90 analyses were obtained from 70 *monazite* crystals from sample VV-4 rich in monazite and used for dating (see below). The bulk-rock composition of this sample (VV-4) shows the ratio $CaO/Na_2O=0.47$ whereas that of V-9 containing only minor amount of monazite is 1.07. Monazite exhibits a rather uniform composition, with low concentrations of Th (1–6, max 10.4 wt% ThO_2), U (0.3–0.55 wt% UO_2) and Y (1–1.6 wt% Y_2O_3). The normalized REE patterns also show monotonous contents of LREE and slightly negative Eu anomalies (Eu/Eu*=0.6–0.9). Uranium correlates with Y due to their similar ionic radii. Representative analyses of allanite and monazite are in Table 3. Several monazite crystals occurring within muscovite and biotite aggregates were chosen for X-ray mapping. The maps od Th, U, and La are shown in Fig. 8. Among these elements only Th shows more pronounced inhomogeneities in accord with its larger Th concentration range. Higher Th concentrations occur irregularly both in centres and rims of the crystals.

Dating of monazite

A total of 90 analysed spots of monazite (one contaminated was excluded) from four thin sections of sample VV-4 were dated, yielding a weighted mean Th–U–total Pb age of 96±3 Ma and MSWD=1.5 (Fig. 9). Excluding another 4 spots below 70 Ma and above 135 Ma gives the same age 95.8±2.7 Ma with MSWD=1.1. Thus, the compositionally homogeneous monazites provide consistent Cretaceous age. Two spots of monazite dated in sample V-9 gave 94 Ma and 131 Ma age. The absence of any older (Variscan) ages strongly suggests that the entire monazite population is a product of Alpine metamorphism.

Metamorphic P–T conditions

Metamorphic *P–T* conditions were calculated using thermodynamic modelling and zirconium-in-rutile geothermometry. Pseudosections were calculated using GeoPS (Xiang & Connolly 2021) with the internally consistent thermodynamic dataset of Holland & Powell (1998) updated in 2004 (HP04. DS). The bulk composition was determined from the XRF whole-rock analysis. The activity-composition models for garnet (White et al. 2007), white mica, biotite, chlorite, cordierite, chloritoid, staurolite, ilmenite (White et al. 2014), feldspar (Holland & Powell 2003) and epidote (Holland & Powell 1998) were used in calculations. We also used zirconium-in-rutile geothermometer (Tomkins et al. 2007), calculating temperature from the Zr content in rutiles. The *P–T* sections

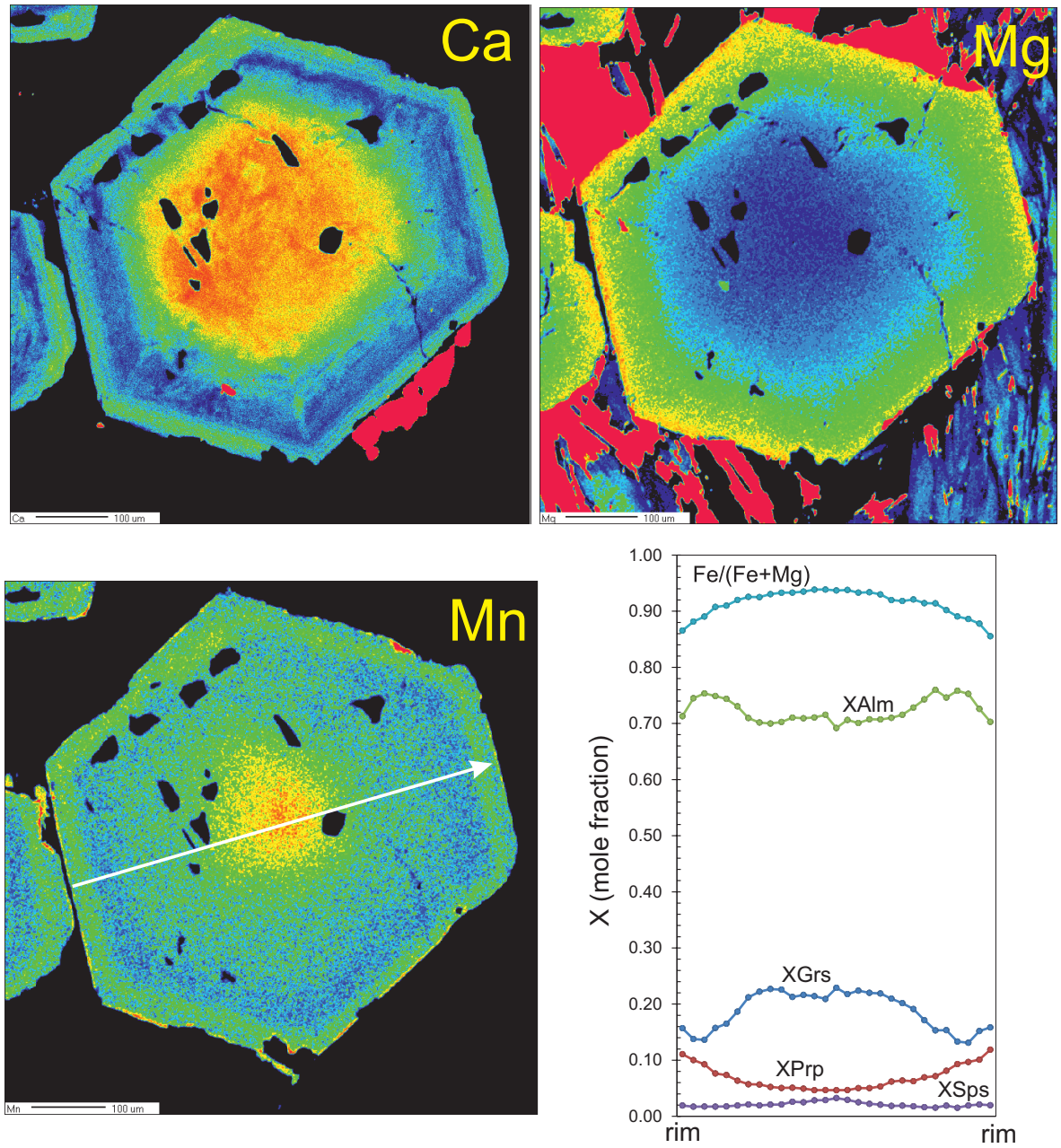

Fig. 4. X-ray maps and compositional profile of garnet (sample V-9) showing distribution of Ca,Mg and Mn in the maps, and X_{Prp}, X_{Grs}, X_{Alm}, X_{Sps} and Fe/(Fe+Mg) across garnet.

were calculated in the system NCKFMMnASTHO assuming H_2O fluid in excess, in the *P–T* range of 500–700 °C and 2–16 kbar. Given the accessory modal amount of allanite (REE-epidote), the amount of excess oxygen (O_2) necessary for stabilization of epidote (a proxy for allanite) was estimated to 0.02–0.025 wt%, corresponding to the FMQ buffer according to the calculated *T* vs. log fO_2 section. The effect of fractionation due to garnet growth was tested using an effective bulk composition (EBC) obtained by subtracting garnet cores. The resulting differences considering phase boundaries and locations of isopleth intersections were minimal and therefore the analysed whole-rock composition without EBC corrections was used to compute the presented pseudosections.

The P–T section of sample V-9 (Fig. 10a) was calculated from the whole-rock composition Na_2O=0.97, MgO=2.05, Al_2O_3=19.84, SiO_2=59.6, K_2O=4.63, CaO=1.04, FeO=7.12, TiO_2=0.79, MnO=0.24 wt%. The stability of allanite approximated by epidote–zoisite field and garnet modes (1–2 vol%) are depicted by lines.

To calculate the peak *P–T* conditions the compositional isopleths of garnet rim (X_{Prp}=0.12, X_{Grs}=0.16–17), phengitic

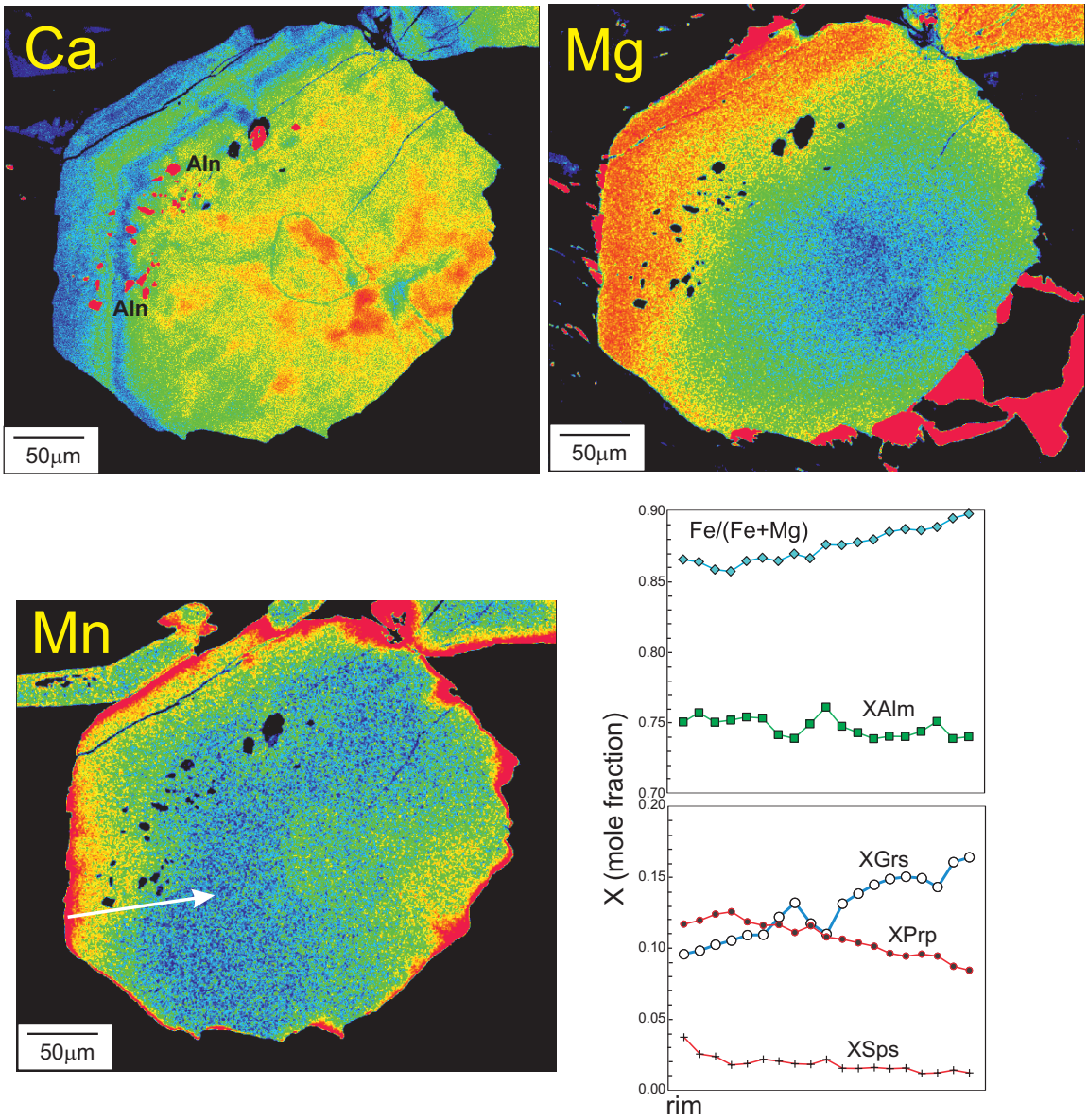

Fig. 5. X-ray maps and compositional profile of garnet (sample VV-4) showing distribution of Ca,Mg and Mn in the maps, and X_{Prp}, X_{Grs}, X_{Alm}, X_{Sps} and Fe/(Fe+Mg) in profile. Note Ca-rich annulus near the allanite (Aln) inclusions.

muscovite (Si=3.2 a.p.f.u.) and biotite (TiO_2=1.5 wt%) corresponding to the measured ones (Tables 1, 2) intersect in the stability field of biotite+garnet+muscovite+paragonite +rutile, which is considered to be the peak mineral assemblage. The measured Zr concentrations in rutile range from 74 to 110 ppm. The average concentration of 96 ppm yields temperature of 566 °C at 10 kbar and 582 °C at 14 kbar. Maximum Zr concentration of 110 ppm yields 575 °C at 10 kbar and 591 °C at 14 kbar. These results suggest a prograde *P–T* path and burial from the stability field of allanite (epidote–zoisite) to peak pressure conditions of 12–14 kbar and 560–600 °C. This was followed by post-burial decompression to ca. 6 kbar, in the stability field of biotite+garnet +ilmenite+muscovite+plagioclase+staurolite, inferred from the occurrence of staurolite in the matrix. Some post-burial heating to 600–610 °C was presumably a consequence of thermal relaxation of the geotherm after crustal thickening.

The P–T section of sample VV-4 shown on Figure 10b was calculated from the whole rock composition Na_2O=1.16, MgO=1.44, Al_2O_3=17.44, SiO_2=66.52, K_2O=3.57, CaO=0.54, FeO=5.58, TiO_2=0.77, MnO=0.1 wt%. The stability of allanite approximated by epidote–zoisite field and garnet modes (1–2 vol%) are depicted by lines.

Compositional isopleths of garnet rim (X_{Prp}=0.12, X_{Grs}=0.12–0.13), phengitic muscovite (Si=3.2 a.p.f.u.) and biotite (TiO_2=1.5 wt%) corresponding to the measured ones (Tables 1, 2) intersect in the stability fields of biotite+garnet +muscovite+paragonite+rutile, and biotite+garnet+muscovite+paragonite+ilmenite+rutile. Since rutile is partly replaced by ilmenite, Zr-in-rutile thermometry was not

Table 2: Representative analyses of micas.

	V-9/96 Mus	V-9/96 Mus	VV-4 Mus	VV-4 Mus	V-9/96 Pa	V-9/96 Pa	VV-4 Pa	VV-4 Pa	V-9/96 Bt	V-9/96 Bt	VV-4 Bt	VV-4 Bt
SiO_2	49.01	49.07	47.94	47.78	47.63	48.65	47.3	47.23	38.16	37.62	36.27	36.85
TiO_2	0.47	0.29	0.37	0.45	0.04	0.06	0.14	0.09	1.58	1.47	1.45	1.64
Al_2O_3	32.97	33.13	31.57	32.86	39.68	40.21	38.88	39.19	19	19.13	18.59	18.32
FeO	1.76	1.65	2.83	2.51	0.26	0.24	0.83	0.69	15.4	17.52	18.98	18.5
MnO	0.01	0	0.01	0	0	0	0	0	0.02	0.07	0.04	0.03
MgO	1.85	1.78	1.62	1.09	0.04	0.09	0.09	0.08	12.66	11.28	10.01	10.16
CaO	0.02	0.01	0.02	0	0.25	0.28	0.22	0.27	0.04	0.02	0.02	0.02
Na_2O	1.15	1.15	1.21	1.36	6.31	5.91	6.72	6.69	0.29	0.23	0.15	0.38
K_2O	9.67	9.4	9.44	9.05	1.37	1.18	1.2	0.94	8.9	8.91	10.19	9.22
Total	96.91	96.48	95.01	95.1	95.58	96.62	95.38	95.18	96.05	96.25	95.7	95.12
Calculated to 11 oxygens												
Si	3.198	3.207	3.210	3.182	3.028	3.047	3.027	3.021	2.797	2.782	2.750	2.786
Ti	0.023	0.014	0.019	0.023	0.002	0.003	0.007	0.004	0.087	0.082	0.083	0.093
Al	2.536	2.553	2.492	2.580	2.974	2.969	2.933	2.955	1.642	1.668	1.662	1.633
Fe	0.096	0.090	0.158	0.140	0.014	0.013	0.044	0.037	0.944	1.084	1.203	1.170
Mn	0.001	0.000	0.001	0.000	0.000	0.000	0.000	0.000	0.001	0.004	0.003	0.002
Mg	0.180	0.173	0.162	0.108	0.004	0.008	0.009	0.008	1.383	1.243	1.131	1.145
Ca	0.001	0.001	0.001	0.000	0.017	0.019	0.015	0.019	0.003	0.002	0.002	0.002
Na	0.146	0.146	0.157	0.176	0.778	0.718	0.834	0.830	0.041	0.033	0.022	0.056
K	0.805	0.784	0.806	0.769	0.111	0.094	0.098	0.077	0.832	0.841	0.986	0.889
X_{Mg}	0.65	0.66	0.50	0.44	0.22	0.40	0.16	0.17	0.59	0.53	0.48	0.49

applied. A prograde *P–T* path from the stability field of allanite (epidote–zoisite) to peak pressure conditions (12–14 kbar, 560–600 °C) is inferred. Post-burial decompression to ca. 6 kbar is inferred from the occurrence of plagioclase in the matrix.

Thermodynamic modelling results suggest that both samples shared similar *P–T* evolution. Replacement of allanite by monazite by rising temperature near peak metamorphic conditions is inferred (Fig. 10a, b). However, as discussed below, allanite-monazite evolution was controlled also by the bulk-rock composition.

Discussion

Allanite–monazite: textural and age relations

Direct allanite–monazite relations are only rarely observed because both REE minerals mostly occur as sole phases, allanite enclosed by garnet, monazite in the matrix mica (biotite, muscovite, paragonite, chlorite) aggregates. In Figure 6a, b monazite grows at rims of allanite clusters suggesting its origin from the allanite. Most of analysed and dated monazites occurring in micas, however, do not seem to have originated by direct replacement of allanite. Absence of apatite (sample VV-4) and higher monazite Th contents also indicate that metamorphic monazite crystallized within its stability field as a sole LREE phase after breakdown of earlier allanite.

Unlike the matrix allanite those armoured by garnet were prevented from replacing by monazite. Dominant monazite crystallization observed in the matrix, and relatively low garnet content (6–7 vol%) can explain why peak monazite was not found in garnet rims.

Association of monazite with xenotime (Fig. 6g, h) enables the application of Y-in-Mnz thermometry. The thermometer of Seydoux-Guillaume et al. (2002) gives an average of 530±24 °C (n=85). Allanite stability approximated by epidote field in pseudosections (Fig. 10a, b) indicates its maximum temperature of 540–560 °C at 6–8 kbar. However, the stability field of allanite is expected to be wider than that of epidote (Janots et al. 2007; Hoschek 2016). This could also explain allanite stability until near peak *P–T* conditions, which correspond to garnet rim composition containing allanite inclusions. The Ca-rich annulus in garnet rim (Fig. 5) indicates an increase of Ca from the allanite breakdown due to a prograde allanite-to-monazite transition (Yang & Pattison 2006; Gieré et al. 2011; Skrzypek et al. 2014). This is supported by the presence of allanite inclusions at, or near, the Ca-rich annulus (Fig. 5). The obtained age of 96 Ma refers, therefore, to the prograde metamorphic stage, probably close to peak *P–T* conditions. The absence of older than Alpine monazite ages in the investigated samples also means that *P–T* conditions of an older (Variscan) metamorphism have not exceeded the allanite/monazite boundary and there is no evidence for recrystallization of older monazite. While the allanite–REE epidote enclosed by garnet (Fig. 6c) undoubtedly grew during prograde garnet growth, the clusters in the matrix might contain older allanite remnants (Fig. 6a). However, the comparison with Alpine and pre-Alpine allanites from the Central Alps as characterised by U/Th and La/Sm ratios (Fig. 11) after Gregory et al. (2012), shows that all analysed grains have low values typical for Alpine allanites.

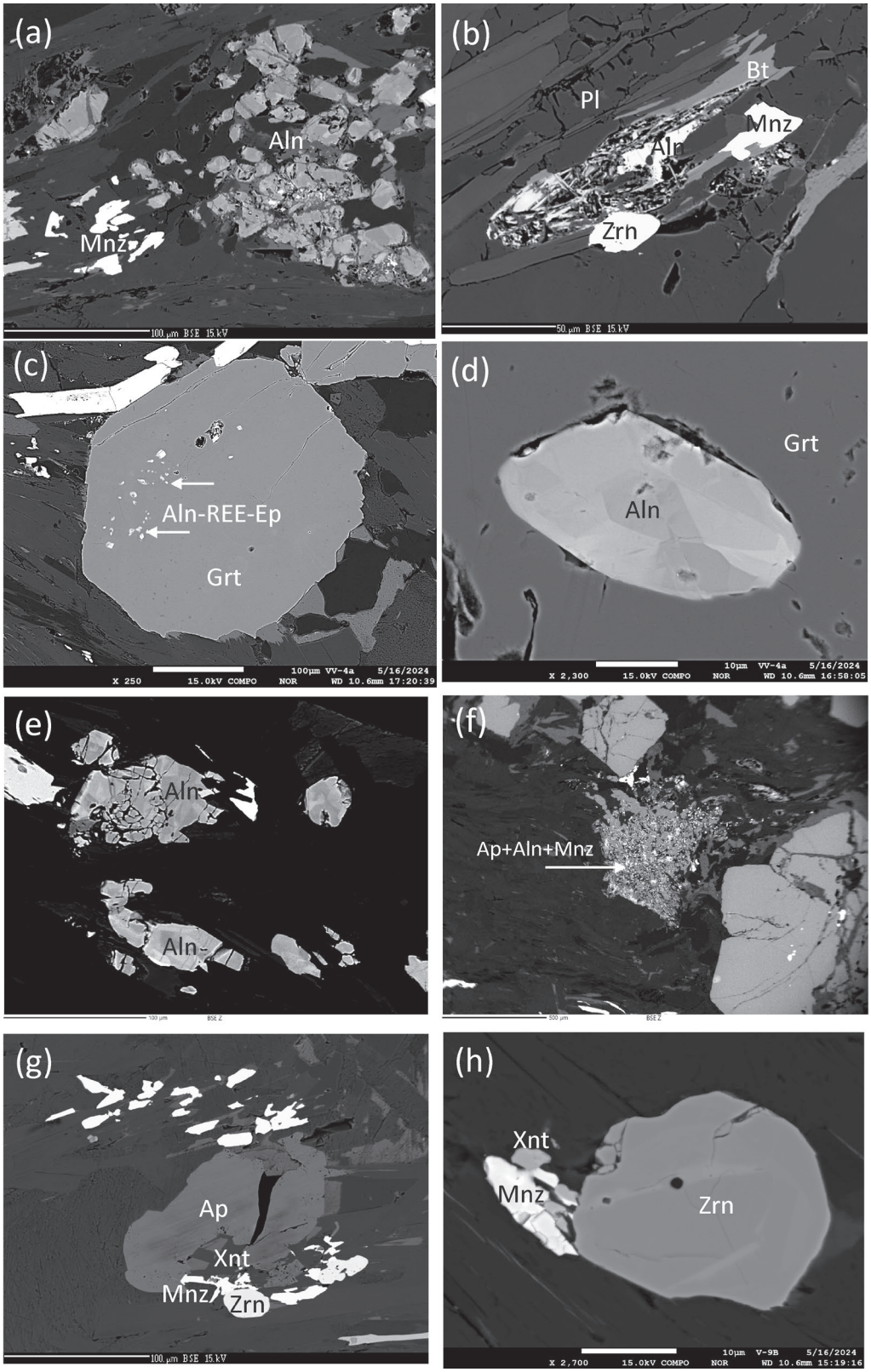

Fig. 6. Back-scattered electron images of allanite and monazite. **a** — Allanite cluster partly replaced by monazite in sample VV-4. **b** — Allanite –REE epidote (REE-ep) rimmed by monazite (Mnz) in the matrix with plagioclase (Pl) and biotite (Bt) in sample VV-4. **c** — Garnet enclosing a cluster of allanites and REE-epidotes in sample VV-4. **d** — Allanite showing a sector zoning enclosed by garnet in sample VV-4. **e** — Allanite and monazite in the matrix chlorite (sample V-9). **f** — Apatite (Ap)–allanite cluster rimmed by monazite in the matrix (sample V-9). **g** — Apatite rimmed by monazite and xenotime (Xnt) in sample VV-4. **h** — Monazite, zircon (Zrn) and xenotime in the matrix muscovite (sample VV-4).

Table 3: Representative analyses of allanite and monazite.

sample	VV-4c	VV-4A	VV-4b	VV-4b	V-9b sv	V-9b		VV-4c	VV-4c	VV-4c	VV-4c	VV-4d	VV-4d
point	aln 1	aln 5	aln 6	aln 7	aln 2	aln 4		mnz 14/2	mnz 26/1	mnz 34/1	mnz 35/1	mnz 37/1	mnz 47/1
SiO_2	34.07	33.31	37.28	33.20	35.11	34.54	SiO_2	0.00	0.00	0.00	0.07	0.04	0.00
TiO_2	0.05	0.08	0.02	0.00	0.04	0.02	TiO_2						
Al_2O_3	20.78	20.51	24.86	20.03	23.80	23.16	Al_2O_3						
FeO	8.03	7.25	1.10	7.81	6.05	5.97	FeO	0.41	0.11	0.09	0.10	0.07	0.31
Fe_2O_3	3.43	4.79	10.57	4.76	4.09	4.51	Fe_2O_3						
MnO	0.52	0.64	0.12	0.48	0.11	0.68	MnO						
MgO	0.21	0.09	0.13	0.47	0.30	0.19	MgO						
CaO	14.33	14.33	21.93	13.51	16.73	15.78	CaO	0.69	0.54	0.53	0.79	0.77	0.46
SrO	0.05	0.29	0.22	0.06	0.18	0.31	SrO	0.01	0.01	0.01	0.01	0.01	0.00
UO_2	0.02	0.08	0.10	0.05	0.20	0.11	UO_2	0.54	0.46	0.38	0.42	0.44	0.48
P_2O_5	0.20	0.10	0.04	0.06	0.04	0.01	P_2O_5	28.51	29.02	28.95	28.76	29.16	29.16
La_2O_3	3.63	3.88	0.50	3.87	2.72	2.84	La_2O_3	14.60	14.71	14.78	14.13	14.50	15.37
Ce_2O_3	7.49	6.71	1.04	8.73	5.59	5.65	Ce_2O_3	29.43	29.07	29.30	28.78	28.68	29.35
Pr_2O_3	0.94	0.70	0.10	0.88	0.64	0.56	Pr_2O_3	2.90	2.91	2.98	2.83	2.92	2.82
Nd_2O_3	3.18	2.60	0.56	3.73	2.38	2.17	Nd_2O_3	12.02	12.20	12.38	11.96	12.08	11.72
Sm_2O_3	0.63	0.42	0.11	0.68	0.42	0.39	Sm_2O_3	2.15	2.21	2.32	2.15	2.17	2.11
Eu_2O_3	0.42	0.11	0.02	0.00	0.01	0.08	Eu_2O_3	0.43	0.38	0.42	0.36	0.41	0.39
Gd_2O_3	0.36	0.55	0.12	0.35	0.20	0.40	Gd_2O_3	1.70	1.71	1.75	1.55	1.58	1.58
Tb_2O_3	0.08	0.07	0.00	0.02	0.06	0.07	Tb_2O_3	0.16	0.25	0.19	0.23	0.26	0.25
Dy_2O_3	0.21	0.03	0.04	0.15	0.02	0.25	Dy_2O_3	0.38	0.36	0.40	0.40	0.38	0.33
Ho_2O_3	0.06	0.00	0.00	0.00	0.00	0.05	Ho_2O_3	0.00	0.01	0.02	0.05	0.06	0.03
PbO							PbO	0.03	0.02	0.02	0.02	0.03	0.02
ThO_2	0.45	0.10	0.06	0.16	0.90	0.08	ThO_2	3.16	2.73	1.78	3.41	3.61	2.26
Y_2O_3	0.55	0.64	0.04	0.46	0.05	1.37	Y_2O_3	1.41	1.38	1.39	1.48	1.34	1.28
SO_3							SO_3	0.03	0.02	0.02	0.02	0.02	0.03
H_2Oc	1.66	1.69	1.86	1.66	1.75	1.73							
Total	101.35	98.95	100.83	101.12	101.37	100.89	Total	98.56	98.11	97.70	97.51	98.53	97.98
Calculated to 12.5 oxygens							Calculated to 4 oxygens						
Si (T3)	2.992	2.977	2.971	2.963	2.969	2.954	P	0.974	0.987	0.987	0.983	0.986	0.990
Ti	0.003	0.005	0.001	0.000	0.002	0.001	Si	0.000	0.000	0.000	0.003	0.002	0.000
Al	2.152	2.161	2.334	2.107	2.372	2.335	T(1)	0.974	0.987	0.987	0.986	0.988	0.990
Fe^{2+}	0.590	0.542	0.073	0.583	0.428	0.427	Ca	0.030	0.023	0.023	0.034	0.033	0.020
Fe^{3+}	0.227	0.322	0.634	0.320	0.260	0.291	Fe	0.014	0.004	0.003	0.003	0.002	0.010
Mn	0.039	0.049	0.008	0.036	0.008	0.049	Th	0.029	0.025	0.016	0.031	0.033	0.021
Mg	0.028	0.012	0.016	0.063	0.038	0.024	U	0.005	0.004	0.003	0.004	0.004	0.004
M(1–3)	3.038	3.092	3.067	3.109	3.108	3.126	Pb	0.000	0.000	0.000	0.000	0.000	0.000
Ca	1.348	1.372	1.872	1.292	1.516	1.446	La	0.217	0.218	0.220	0.211	0.214	0.227
U	0.000	0.001	0.002	0.001	0.004	0.002	Ce	0.435	0.428	0.432	0.425	0.420	0.431
P	0.015	0.007	0.003	0.005	0.003	0.001	Pr	0.043	0.043	0.044	0.042	0.043	0.041
Na	0.014	0.005	0.000	0.000	0.000	0.000	Nd	0.173	0.175	0.178	0.172	0.172	0.168
La	0.118	0.128	0.015	0.127	0.085	0.090	Sm	0.030	0.031	0.032	0.030	0.030	0.029
Ce	0.241	0.220	0.030	0.285	0.173	0.177	Eu	0.006	0.005	0.006	0.005	0.006	0.005
Pr	0.030	0.023	0.003	0.029	0.020	0.017	Gd	0.023	0.023	0.023	0.021	0.021	0.021
Nd	0.100	0.083	0.016	0.119	0.072	0.066	Tb	0.002	0.003	0.003	0.003	0.003	0.003
Sm	0.019	0.013	0.003	0.021	0.012	0.012	Dy	0.005	0.005	0.005	0.005	0.005	0.004
Eu	0.012	0.003	0.000	0.000	0.000	0.002	Ho	0.000	0.000	0.000	0.001	0.001	0.000
Gd	0.011	0.016	0.003	0.010	0.006	0.011	Y	0.030	0.029	0.030	0.032	0.029	0.027
Tb	0.002	0.002	0.000	0.001	0.002	0.002	Total	2.021	2.008	2.011	2.011	2.008	2.009
Dy	0.006	0.001	0.001	0.004	0.001	0.007	X LREE	0.875	0.884	0.894	0.866	0.869	0.894
Ho	0.002	0.000	0.000	0.000	0.000	0.001	X HREE	0.034	0.036	0.035	0.034	0.034	0.034
Th	0.009	0.002	0.001	0.003	0.017	0.001	X hutt	0.004	0.006	0.000	0.001	0.004	0.005
Y	0.026	0.030	0.002	0.022	0.002	0.062	X cher	0.057	0.046	0.045	0.067	0.065	0.039
A(1–2)	1.953	1.907	1.951	1.919	1.912	1.898	X xnt	0.029	0.029	0.029	0.031	0.028	0.027
Total	7.983	7.976	7.988	7.991	7.989	7.978	T,°C	532.2	538.7	539.3	544.3	525.5	513.9

Note: Allanite points aln 5 (VV-4) and aln 2 (V-9) are inclusions in garnet. Point aln 6 (VV-4) corresponds to REE epidote.
Temperatures in mnz are calculated after Seydoux-Guillaume et al. (2002)
H_2Oc: H_2O calculated according to allanite stoichiometry

Allanite–monazite: bulk-rock composition

It is generally known that during prograde metamorphism allanite transforms to monazite in metapelites whose bulk-rock composition shows low CaO/Na_2O ratios, whereas in samples of intermediate to high CaO/Na_2O ratios allanite is preserved (Janots et al. 2008).

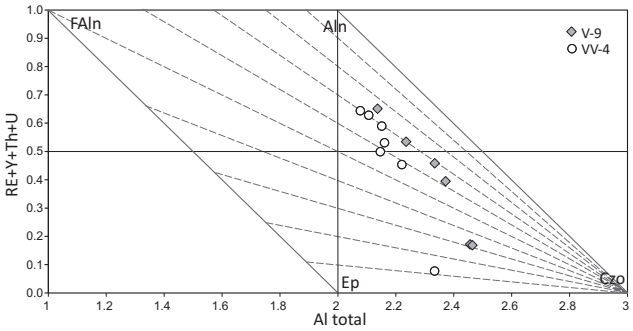

Fig. 7. Major element allanite–REE epidote compositions showing V-9 sample shifted to more Al rich composition (plot after Petrík et al. 1995).

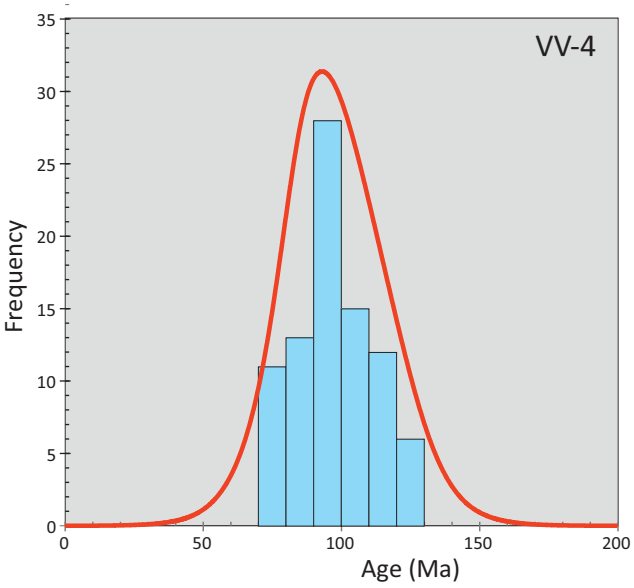

Fig. 9. Histogram and probability density plot for monazite ages (n=85), weighted mean 96±3 Ma. PDP calculated by Isoplot 4.15 (Ludwig 2012).

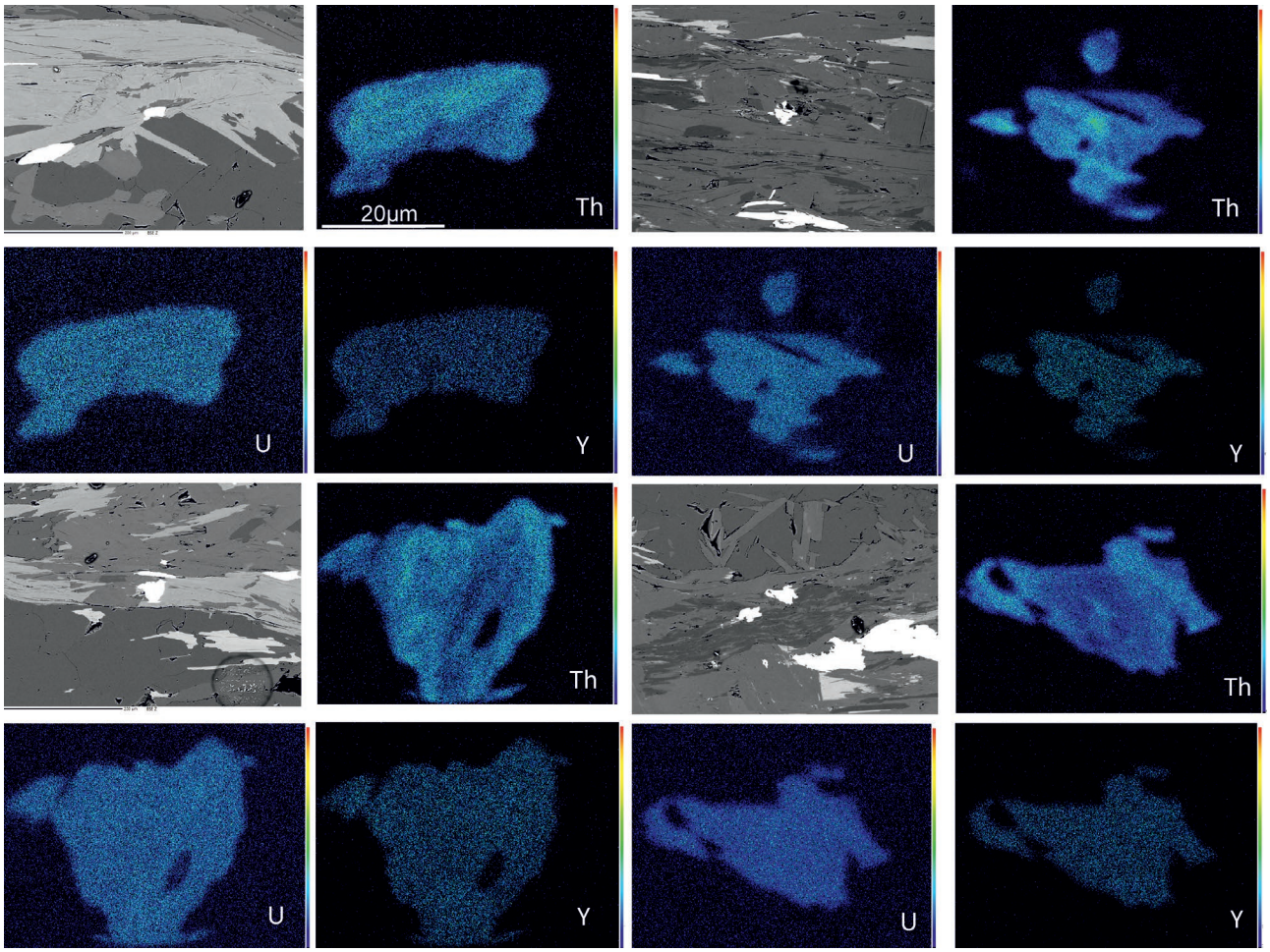

Fig. 8. X-ray maps of matrix monazites from sample VV-4. The only significant zoning is shown by Th.

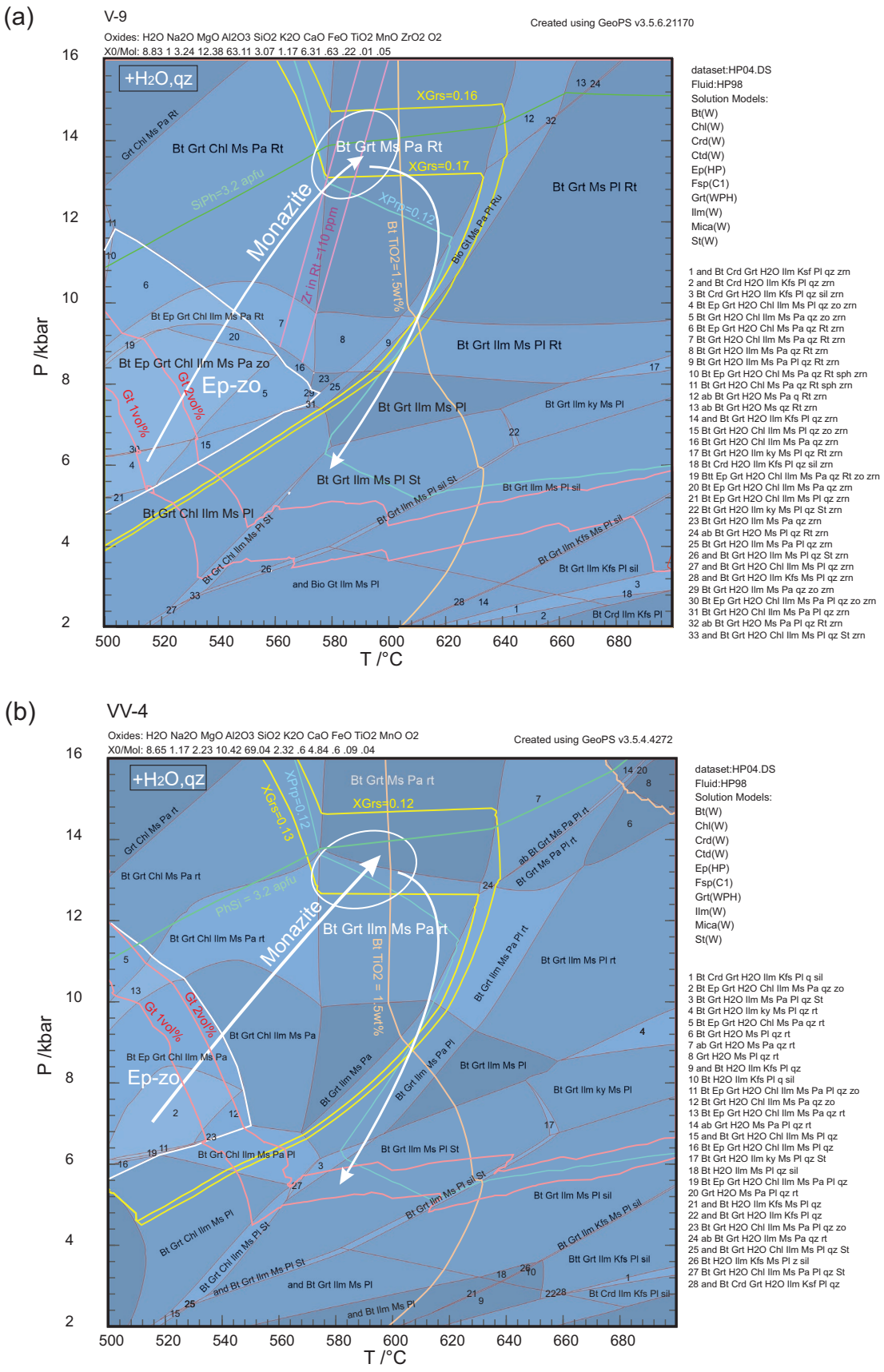

Fig. 10. *P–T* phase diagrams for sample V-9 (**a**), and sample VV-4 (**b**). The arrows show the *P–T* paths constrained by thermodynamic modelling and considering allanite-monazite evolution. See the text for details.

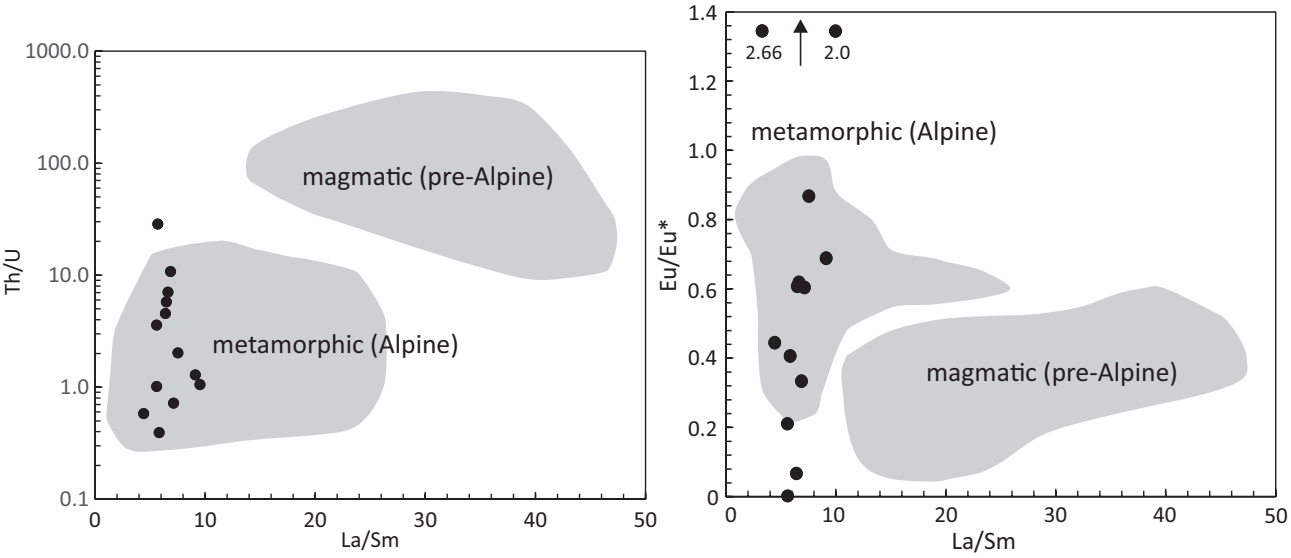

Fig. 11. Allanite compositions (sample VV-4) compared with the fields of pre-Alpine and Alpine allanites from the Central Alps according to Gregory et al. (2012).

The effect of bulk-rock composition clearly controls the allanite–monazite relationships in the studied samples from the Veporic unit (Fig. 12). The bulk-rock composition of sample VV-4 containing abundant monazite shows the ratio $CaO/Na_2O=0.47$, whereas that of V-9 containing minor amount of monazite is 1.07. This means that formation of monazite from allanite was controlled by low-Ca bulk-rock composition which is not the case for the majority of lithologies in the Veporic unit, thus limiting the occurrence of monazite and its use for dating.

In general, prograde allanite–monazite–garnet relations observed in the investigated metapelites from the southern Veporic unit resemble those described by Janots et al. (2008) from the Central Alps or Skrzypek et al. (2017) from the Orlica–Śnieżnik Dome in the Sudetes, among others.

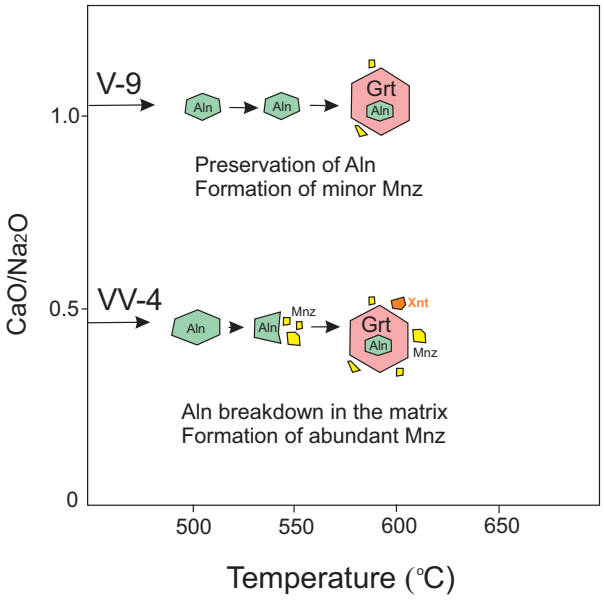

Fig. 12. Prograde metamorphic sequence of allanite, monazite and xenotime as a function of temperature and CaO/Na_2O ratio (see the text). Modified from Janots et al. (2008).

Tectonic implications

The southern Veporic zones represent a metamorphic dome with downward-increasing pressure–temperature conditions. The pervasive syn-metamorphic foliation in both the cover and in underlying basement granitoids is generally subhorizontal in the centre of the dome and flatly northeast- to southeast-dipping along its eastern flanks. The stretching lineation is either horizontal in the centre, or slightly ENE-plunging (Plašienka 1993; Janák et al. 2001; Jeřábek et al. 2007, 2012). The overall kinematic framework includes NW–SE shortening and SW–NE orogen-parallel stretching that was finalized by doming and exhumation by eastward-directed, low-angle unroofing of the metamorphic core (Plašienka 1993; Janák et al. 2001; Bukovská et al. 2013; Potočný et al. 2020). This tectonic evolution was controlled by two crustal thickening events – first hangingwall overthrusting by the Gemeric and higher units, and second footwall underthrusting of the foreland Fatric basement (Plašienka 1997, 2018; Lexa et al. 2003; Jeřábek et al. 2012; Fig. 13).

The syn-burial metamorphic foliation developed under increasing pressure–temperature conditions up to 12–14 kbar and 580–600 °C which is consistent with previous *P–T* estimates (Janák et al. 2001; Jeřábek et al. 2008) in the deepest exposed complexes of the Veporic unit.

The prograde metamorphism between 100–95 Ma in the deeply buried Veporic complexes is documented by geochronological data. This is indicated by the post-kinematic growth

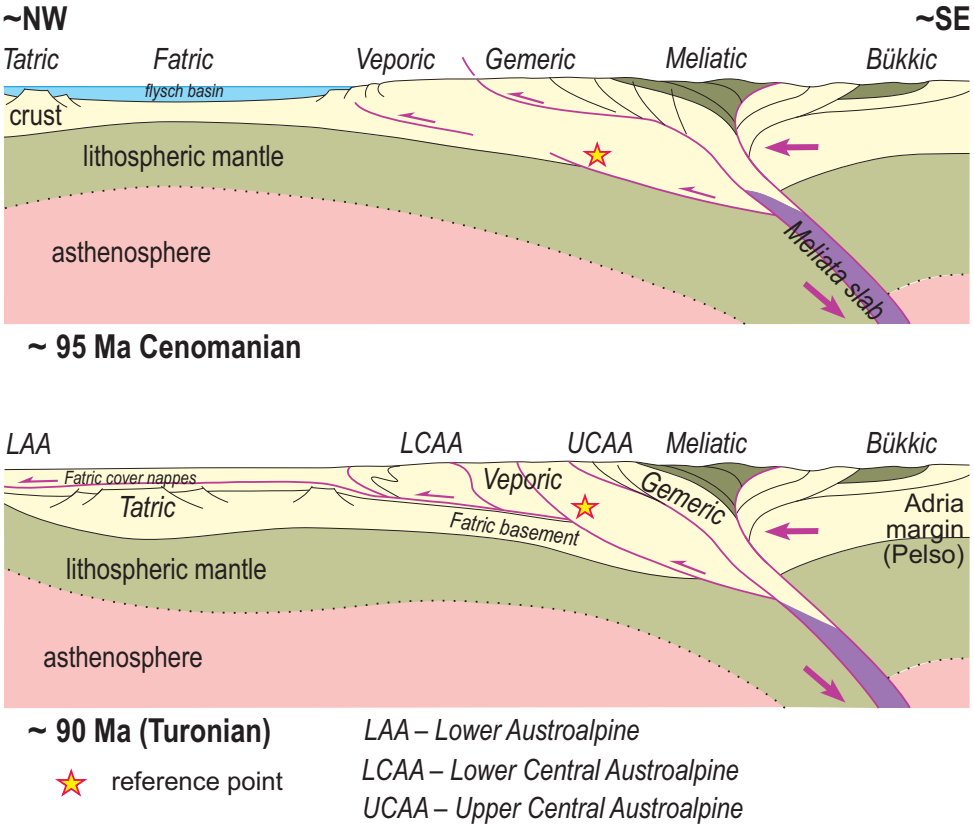

Fig. 13. The tectonic scenario for the burial and exhumation of the Veporic metamorphic complex. The upper cross-section shows situation after overthusting by the Gemeric and higher units that caused metamorphism in the underlying Veporic unit. The lower cross-section illustrates underthrusting of the Fatric crust and start of fold-induced exhumation of the Veporic unit that was followed by orogen-parallel unroofing by low-angle detachment faulting perpendicular to the cross-section plane. Correlation with tectonic superunits in the Eastern Alps is indicated (LAA etc.).

of monazite in the southern Veporic cover dated to 97±4 Ma by the laser ablation ICP-MS method (Bukovská et al. 2013), and here presented U–Th–Pb monazite age data of 96 Ma from the southern Veporic basement. The subsequent exhumation is dated by various cooling ages from ca 90 to 55 Ma (e.g., Janák et al. 2001; Dallmeyer et al. 2005; Putiš et al. 2009; Vojtko et al. 2016, 2017) accompanied by intrusion of the post-kinematic Rochovce granite at 75–76 Ma (Poller et al. 2001) or 81–82 Ma (Kohút et al. 2013).

Correlations with the Austroalpine units of the Eastern Alps

The above described tectono-metamorphic scenario for the southern Veporic zones implies certain correlation aspects with the Austroalpine units of the Eastern Alps. In particular, there are several hints to connect the Veporic unit with the Lower Central Austroalpine units (LCAA; Janák et al. 2004; formerly known as the Middle Austroalpine). The LCAA pre-Alpine basement complexes experienced the Permian thermal event related to gabbroic intrusions, especially in the internal, southern parts, and a southwards increasing Eo-Alpine metamorphic overprint from greenschist to eclogite facies. Several LCAA units have been distinguished (Schmid et al. 2004; Froitzheim et al. 2008): (1) the lowermost Silvretta–Seckau nappe system; (2) the Koralpe–Wöltz basement nappes that underwent a high-grade Eo-Alpine overprint up to the eclogite facies (Sieggraben, Kreuzeckgruppe, Saualpe–Koralpe, Pohorje complexes); (3) the Ötztal–Bundschuh nappe system affected by upward decreasing Eo-Alpine metamorphism from amphibolite to greenschist facies conditions. On the other hand, the Upper Central Austroalpine basement-involved nappe system (UCAA) includes the Drauzug–Gurktal nappe system and the Northern Greywacke Zone, partially correlative with the WeCa Gemeric units (Fig. 13).

The Eastern Alpine High-Pressure Belt (EAHPB, Fig. 1) is characterized by the Eo-Alpine HP–UHP metamorphic overprint. As proposed by Balla (1994), Schmid et al. (2004), and Plašienka & Bielik (2024), the EAHPB could continue eastward beneath the Neogene deposits of the Danube Basin system as a zone of positive gravity and magnetic anomalies. These anomalies are thought to be generated by dense bodies of ultramafic and/or eclogitic rocks. In the Slovenian Pohorje Mts, the ultra-high pressure metamorphic complexes (UHPC in Fig. 1) include diamond-bearing paragneisses, kyanite eclogites, ultramafics and garnet peridotites (Janák et al. 2004,

2006, 2015; Vrabec et al. 2012). The tectonic evolution of the UHPC progressed from deep intra-continental subduction, exhumation by slab extraction, exhumation-related folding and finally by core-complex style of N–S shortening and E-directed extensional unroofing (Janák et al. 2004; Kirst et al. 2010; Chang et al. 2020). Cretaceous metamorphic domes with very similar characteristics to the southern Veporic dome are also present in the other regions of LCAA (e.g., the Gleinalm dome; Neubauer et al. 1995). The timing of metamorphism at ca. 96 Ma in the Veporic Unit is in excellent agreement with the Eo-Alpine intracontinental subduction and HP/UHP metamorphism between 100 and 90 Ma in the Austroalpine Nappes of the Eastern Alps (Janák et al. 2004; Stüwe & Schuster 2010; Miladinova et al. 2021 and references therein).

Conclusions

- Formation of monazite from allanite in the garnet mica schists from the Veporic unit (Western Carpathians) is recorded by early allanite enclosed in garnet cores and newly formed monazite partly replacing allanite in the chlorite, muscovite, and biotite matrix.
- Monazite formation was controlled by rising temperature and low-Ca bulk-rock composition along a prograde *P–T* path from ca. 6–8 kbar and 520–550 °C to 12–14 kbar and 580–600 °C.
- Dating of monazite yielded an age of 95.8±2.7 Ma which refers to the prograde metamorphic stage, probably close to the peak of metamorphism.
- Prograde metamorphism was related to burial of the Veporic unit in the Late Cretaceous, coeval with the Eo-Alpine HP/UHP metamorphism (100–90 Ma) in the Austroalpine Nappes, which supports the correlation with intracontinental subduction in the Eastern Alps.

Acknowledgements: We thank E. Skrzypek, P. Jeřábek and R. Vojtko for their reviews. This work was supported by the Slovak Research and Development Agency under grant projects APVV-18-0107, APVV-21-0281 and Scientific grant agency VEGA (projects 2/0002/24, 1/0021/25).

References

Balla Z. 1994: Basement tectonics of the Danube Lowlands. *Geologica Carpathica* 45, 271–281.

Biely A. 1956: Príspevok ku geológii okolia Dobšinej [Beitrag zur Geologie der Umgebung von Dobšiná]. *Geologické práce, Zprávy* 5, 37–60 (in Slovak with German summary).

Bukovská Z., Jeřábek P., Lexa O., Konopásek J., Janák M. & Košler J. 2013: Kinematically unrelated C-S fabrics: an example of extensional shear band cleavage from the Veporic Unit (Western Carpathians). *Geologica Carpathica* 64, 103–116. https://doi.org/10.2478/geoca-2013-0007

Chang R., Neubauer F., Liu Y., Genser J., Jin W., Yuan S., Guan Q., Huang Q. & Li W. 2020: Subduction of a rifted passive continental margin: the Pohorje case of Eastern Alps–constraints from geochronology and geochemistry. *Swiss Journal of Geociences* 113, 14. https://doi.org/10.1186/s00015-020-00369-z

Dallmeyer R.D., Neubauer F., Handler R., Fritz H., Müller W., Pana D. & Putiš M. 1996: Tectonothermal evolution of the internal Alps and Carpathians: Evidence from $^{40}Ar/^{39}Ar$ mineral and whole-rock data. *Eclogae Geologicae Helvetiae* 89, 203–227.

Dallmeyer R.D., Németh Z. & Putiš M. 2005: Regional tectonometamorphic events in Gemericum and adjacent units (Western Carpathians, Slovakia): Contribution by the $^{40}Ar/^{39}Ar$ dating. *Slovak Geological Magazine* 11, 155–163.

Dallmeyer R.D., Neubauer F. & Fritz H. 2008: The Meliata suture in the Carpathians: regional significance and implications for the evolution of high-pressure wedges within collisional orogens. In: Siegesmund S., Fügenschuh B. & Froitzheim N. (eds.): Tectonic aspects of the Alpine–Dinaride–Carpathian system. *Geological Society, London, Special Publication* 298, 101–115. https://doi.org/10.1144/SP298.6

Froitzheim N., Plašienka D. & Schuster R. 2008: Alpine tectonics of the Alps and Western Carpathians. In: McCann T. (ed.): The Geology of Central Europe. Volume 2: Mesozoic and Cenozoic. *Geological Society Publishing House*, London, 1141–1232.

Gaab A., Janák M., Poller U. & Todt W. 2006: Alpine reworking of Ordovician protoliths in the Western Carpathians: Geochronological and geochemical data on the Muran Gneiss Complex, Slovakia. *Lithos*, 87, 261–275. https://doi.org/10.1016/j.lithos.2005.06.010

Gerátová S., Vojtko R., Lačný A. & Kriváňová K. 2022: The structural pattern and tectonic evolution of the Muráň fault revealed by geological data, fault-slip analysis, and paleostress reconstruction (Western Carpathians). *Geologica Carpathica* 73, 43–62. https://doi.org/10.31577/GeolCarp.73.1.3

Gieré R., Rumble D., Günther D., Connolly J. & Caddick M. 2011: Correlation of growth and breakdown of major and accessory minerals in metapelites from Campolungo, Central Alps. *Journal of Petrology* 52, 2293–2334. https://doi.org/10.1093/petrology/egr043

Gregory C., Rubatto D., Hermann J., Berger A. & Engi M. 2012: Allanite behaviour during incipient melting in the Southern Central Alps. *Geochimica et Cosmochimica Acta* 84, 433–458. https://doi.org/10.1016/j.gca.2012.01.020

Holland T.J.B. & Powell R. 1998: An internally consistent thermodynamic data set for phases of petrological interest. *Journal of Metamorphic Geology* 16, 309–343. https://doi.org/10.1111/j.1525-1314.1998.00140.x

Holland T.J.B. & Powell R. 2003: Activity–composition relations for phases in petrological calculations: An asymmetric multicomponent formulation. *Contributions to Mineralogy and Petrology* 145, 492–501. https://doi.org/10.1007/s00410-003-0464-z

Hoscheck G. 2016: Phase relations of the REE minerals florencite, allanite and monazite in quartzitic granet-kyanite schist of the Eclogite Zone, Tauern Window, Austria. *European Journal of Mineralogy* 28, 735–750. https://doi.org/10.1127/ejm/2016/0028-2549

Janák M., Plašienka D., Frey M., Cosca M., Schmidt S.Th., Lupták B. & Méres Š. 2001: Cretaceous evolution of a metamorphic core complex, the Veporic unit, Western Carpathians (Slovakia): P–T conditions and in situ $^{40}Ar/^{39}Ar$ UV laser probe dating of metapelites. *Journal of Metamorphic Geology* 19, 197–216. https://doi.org/10.1046/j.0263-4929.2000.00304.x

Janák M., Froitzheim N., Lupták B., Vrabec M. & Ravna E.J.K. 2004: First evidence for ultrahigh-pressure metamorphism of eclogites in Pohorje, Slovenia: Tracing deep continental subduction in the Eastern Alps. *Tectonics* 23, TC5014. https://doi.org/10.1029/2004TC001641

Janák M., Froitzheim N., Vrabec M., Krogh Ravna E.J. & De Hoog J.C.M. 2006: Ultrahigh-pressure metamorphism and exhumation of garnet peridotites in Pohorje, eastern Alps. *Journal of Metamorphic Geology* 24, 19–31. https://doi.org/10.1111/j.1525-1314.2005.00619.x

Janák M., Froitzheim N., Yoshida K., Sasinková M., Nosko M., Kobayashi T., Hirajima T. & Vrabec M. 2015: Diamond in metasedimentary crustal rocks from Pohorje, Eastern Alps: a window to deep continental subduction. *Journal of Metamorphic Geology* 33, 495–512. https://doi.org/10.1111/jmg.12130

Janots E., Brunet F., Goffe B., Poinssot C., Burchard M. & Cemič L. 2007: Thermochemistry of monazite-(La) and dissakisite-(La): implications for monazite and allanite stability in metapelites. *Contributions to Mineralogy and Petrology* 154, 1–14. https://doi.org/10.1007/s00410-006-0176-2

Janots E., Engi M., Berger A., Allaz J., Schwartz J.-O. & Spandler C. 2008: Prograde metamorphic sequence of REE minerals in pelitic rocks of the Central Alps: implications for allanite–monazite–xenotime phase relations from 250 to 610 °C. *Journal of Metamorphic Geology* 26, 509–526. https://doi.org/10.1111/j.1525-1314.2008.00774.x

Janots E., Engi M., Rubatto D., Berger A., Gregory C. & Rahn M. 2009: Metamorphic rates in collisional orogeny from in situ allanite and monazite dating. *Geology*, 37, 11–14. https://doi.org/10.1130/G25192A.1

Jeřábek P., Stünitz H., Heilbronner R., Lexa O. & Schulmann K. 2007: Microstructural-deformation record of an orogen-parallel extension in the Vepor Unit, West Carpathians. *Journal of Structural Geology*, 29, 1722–1743. https://doi.org/10.1016/j.jsg.2007.09.002

Jeřábek P., Faryad S.W., Schulmann K., Lexa O. & Tajčmanová L. 2008: Alpine burial and heterogeneous exhumation of Variscan crust in the West Carpathians: insight from thermodynamic and argon diffusion modelling. *Journal of the Geological Society*, 165, 479–498. https://doi.org/10.1144/0016-76492006-165

Jeřábek P., Lexa O., Schulmann K. & Plašienka D. 2012: Inverse ductile thinning via lower crustal flow and fold-induced doming in the West Carpathian Eo-Alpine collisional wedge. *Tectonics* 31, TC5002. https://doi.org/10.1029/2012TC003097

Kirst F., Sandmann S., Nagel T.J., Froitzheim N. & Janák M. 2010: Tectonic evolution of the southeastern part of the Pohorje Mountains (Eastern Alps, Slovenia). *Geologica Carpathica* 61, 451–461. https://doi.org/10.2478/v10096-010-0027-y

Klinec A. 1966: Zum Bau und Bildung des Veporiden-Kristallin. *Sborník geologických vied, rad ZK* 6, 7–28 (in Slovak with German summary).

Klinec A. 1971: The main tectonic elements in the eastern Veporides. *Geologické práce, Správy* 57, 105–109 (in Slovak with English summary).

Klinec A. 1980: Contiguous zone of Gemerides and Veporides enlightened by well near Rochovce. *Geologický zborník – Geologica Carpathica* 31, 537–540.

Kohút M., Stein H., Uher P., Zimmerman A. & Hraško Ľ. 2013: Re–Os and U–Th–Pb dating of the Rochovce granite and its mineralization (Western Carpathians, Slovakia). *Geologica Carpathica* 64, 71–79. https://doi.org/10.2478/geoca-2013-0005

Konečný P., Kusiak M.A. & Dunkley D.J. 2018: Improving U–Th–Pb electron microprobe dating using monazite age references. *Chemical Geology* 484, 22–35. https://doi.org/10.1016/j.chemgeo.2018.02.014

Korikovsky S.P., Janák M. & Boronichin V.A. 1986: Geothermometry and mineral equilibria during recrystallization of garnet mica schists and cordierite-bearing hornfelses in the Rochovce granite aureole (Slovak Ore Mts., Rochovce-Chyžné district). *Geologický zborník – Geologica Carpathica* 37, 607–633 (in Russian with English abstract).

Kozur H. 1991: The evolution of the Meliata-Hallstatt ocean and its significance for the early evolution of the Eastern Alps and Western Carpathians. *Paleogeography, Palaeoclimatology, Palaeoecology* 87, 109–135.

Lexa O., Schulmann K. & Ježek J. 2003: Cretaceous collision and indentation in the West Carpathians: View based on structural analysis and numerical modeling. *Tectonics* 22, 1066.

Ludwig K.R. 2012: User's Manual for Isoplot Version 3.75–4.15: Geochronological Toolkit for Microsoft Excel. *Berkeley Geochronological Center Special Publication*, 5.

Lupták B., Janák M., Plašienka D., Schmidt S.Th. & Frey M. 2000: Chloritoid-kyanite schists from the Veporic unit, Western Carpathians, Slovakia: implications for Alpine (Cretaceous) metamorphism. *Schweizerische Mineralogische und Petrographische Mitteilungen* 80, 213–223.

Lupták B., Janák M., Plašienka D. & Schmidt S.Th. 2003: Alpine low-grade metamorphism of the Permian-Triassic sedimentary rocks from the Veporic superunit, Western Carpathians: phyllosilicate composition and "crystallinity" data. *Geologica Carpathica* 54, 367–375.

Maluski H., Rajlich P. & Matte P. 1993: ^{40}Ar–^{39}Ar dating of the Inner Carpathians Variscan basement and Alpine mylonitic overprint. *Tectonophysics* 223, 313–337.

Méres Š. & Hovorka D. 1991: Geochemistry and metamorphic evolution of the Kohút crystalline complex mica schists (Western Carpathians), *Acta Geologica et Geographica Universitatis Comenianae, Geologica* 47, 15–66.

Miladinova I., Froitzheim N., Nagel Th., Janák M., Fonseca R.O.C., Sprung P. & Münker C. 2021: Constraining the process of intracontinental subduction in the Austroalpine Nappes: Implications from petrology and Lu–Hf geochronology of eclogites. *Journal of Metamorphic Geology* 40, 423–456. https://doi.org/10.1111/jmg.12634

Neubauer F., Dallmeyer R.D., Dunkl I. & Schirnik D. 1995: Late Cretaceous exhumation of the metamorphic Gleinalm dome, Eastern Alps: kinematics, cooling history and sedimentary response in a sinistral wrench corridor. *Tectonophysics*, 242, 79–98.

Petrík I., Broska I., Lipka J. & Siman P. 1995: Granitoid allanite-(Ce):substitutions, redox conditions and REE distributions (on an example of I-type granitoids, Western Carpathians, Slovakia). *Geologica Carpathica* 46, 79–94.

Plašienka D. 1980: Nappe position of the Hladomorná dolina group on the Foederata group in the Dobšiná half-window. *Geologický zborník – Geologica Carpathica* 31, 609–617.

Plašienka D. 1984: Príkrov Markušky – zväzujúci element veporika a gemerika? [Represents the Markuška nappe an interconnecting element between the Veporic and Gemeric units?] *Mineralia Slovaca* 16, 187–193 (in Slovak, English summary).

Plašienka D. 1993: Structural pattern and partitioning of deformation in the Veporic Foederata cover unit (Central Western Carpathians). In: M. Rakús & J. Vozár (eds.): Geodynamic model and deep structure of the Western Carpathians. *Conf., Symp., Sem., D. Štúr Inst. Geol.*, Bratislava, 269–277.

Plašienka D. 1997: Cretaceous tectonochronology of the Central Western Carpathians (Slovakia). *Geologica Carpathica* 48, 99–111.

Plašienka D. 2018: Continuity and episodicity in the early Alpine tectonic evolution of the Western Carpathians: How large-scale processes are expressed by the orogenic architecture and rock record data. *Tectonics* 37, 2029–2079. https://doi.org/10.1029/2017TC004779

Plašienka D. & Bielik M. 2024: The Kolárovo gravity and magnetic anomaly body in a subcrop of the Danube Basin: A new geological interpretation. *Geologica Carpathica* 75, 49–59. https://doi.org/10.31577/GeolCarp.2024.03

Plašienka D. & Soták J. 2001: Stratigrafické a tektonické postavenie karbónskych sedimentov v doline Furmanca (Muránska planina) [Stratigraphic and tectonic position of Carboniferous sediments in the Furmanec Valley (Muráň Plateau, Central Western Carpathians)]. *Mineralia Slovaca* 33, 29–44 (in Slovak with English summary).

Plašienka D., Janák M., Lupták B., Milovský R. & Frey M. 1999: Kinematics and metamorphism of a Cretaceous core complex: the Veporic Unit of the Western Carpathians. *Physics and Chemistry of the Earth (A)* 24, 651–658.

Plašienka D., Méres Š., Ivan P., Sýkora M., Soták J., Lačný A., Aubrecht R., Bellová S. & Potočný T. 2019: Meliatic blueschists and their detritus in Cretaceous sediments: New data constraining tectonic evolution of the West Carpathians. *Swiss Journal of Geosciences* 112, 55–81. https://doi.org/10.1007/s00015-018-0330-7

Plašienka D., Bučová J. & Šimonová V. 2020: Variable structural styles and tectonic evolution of an ancient backstop boundary – the Pieniny Klippen Belt of the Western Carpathians. *International Journal of Earth Sciences* 109, 1355–1376. https://doi.org/10.1007/s00531-019-01789-5

Poller U., Uher P., Janák M., Plašienka D. & Kohút M. 2001: Late Cretaceous age of the Rochovce granite, Western Carpathians, constrained by U-Pb single-zircon dating in combination with cathodoluminiscence imaging. *Geologica Carpathica*, 52, 41–47.

Potočný T., Méres Š. & Plašienka D. 2020: Geological structure and tectonometamorphic evolution of the Veporic–Gemeric contact zone constrained by the monazite age data (Slavošovce–Štítnik area, Western Carpathians, Slovakia). *Mineralia Slovaca* 52, 83–102.

Putiš M. 1991: Geology and petrotectonics of some shear zones in the West Carpathian crystalline complexes. *Mineralia Slovaca* 23, 459–473.

Putiš M., Frank W., Plašienka D., Siman P., Sulák M. & Biroň A. 2009: Progradation of the Alpidic Central Western Carpathians orogenic wedge related to two subductions: constrained by $^{40}Ar/^{39}Ar$ ages of white micas. *Geodinamica Acta* 22, 31–56. https://doi.org/10.3166/ga.22.31-56

Schmid S.M., Fügenschuh B., Kissling E. & Schuster R. 2004: Tectonic map and overall architecture of the Alpine orogen. *Eclogae Geologicae Helvetiae* 97, 93–117.

Seydoux-Guillaume A.M., Paquette J.-L., Wiedenbeck M., Montel, J.-M. & Heinrich W. 2002: Experimental resetting of the U–Th–Pb systems in monazite. *Chemical Geology* 191, 165–181. https://doi.org/10.1016/S0009-2541(02)00155-9

Skrzypek E., Lehman, J., Sczepański J., Anczkiewicz R., Štípská P., Schulmann K., Kroner A. & Bialek D. 2014: Time-scale of deformation and intertectonic phases revealed by *P-T-D-t* relationships in the orogenic middle crust of the Orlica-Śnieżnik Dome, Polish/Scech Central Sudetes. *Journal of Metamorphic Geology* 32, 981–1003. https://doi.org/10.1111/jmg.12103

Skrzypek E., Bosse V., Kawakami T., Martelat J.-E. & Štípská P. 2017: Transient allanite replacement and prograde to retrograde monazite (re)crystallization in medium-grade metasedimentary rocks from the Orlica-Śnieżnik Dome (Czech Republic/Poland): Textural and geochronological arguments. *Chemical Geology* 449, 41–57. https://doi.org/10.1016/j.chemgeo.2016.11.033

Smith H.A, Barreiro B. 1990: Monazite U–Pb dating of staurolite grade metamorphism in pelitic schists. *Contributions to Mineralogy and Petrology* 105, 602–615.

Spear F.S. 2010: Monazite-allanite phase relations in metapelites. *Chemical Geology* 279, 55–62. https://doi.org/10.1016/j.chemgeo.2010.10.004

Stumpf S., Skrzypek E. & Stüwe K. 2024: Dating prograde metamorphism: U–Pb geochronology of allanite and REE-rich epidote in the Eastern Alps. *Contributions to Mineralogy and Petrology* 179, 63. https://doi.org/10.1007/s00410-024-02130-3

Stüwe K. & Schuster R. 2010: Initiation of subduction in the Alps: Continent or ocean? *Geology* 38, 175–178. https://doi.org/10.1130/G30528.1

Tomkins H.S., Powell R. & Ellis D. 2007: The pressure dependence of the zirconium-in-rutile thermometer. *Journal of Metamorphic Geology* 25, 703–713. https://doi.org/10.1111/j.1525-1314.2007.00724.x

Vojtko R., Králiková S., Jeřábek P., Schuster R., Danišík M., Fügenschuh B., Minár J. & Madarás J. 2016: Geochronological evidence for the Alpine tectono-thermal evolution of the Veporic Unit (Western Carpathians, Slovakia). *Tectonophysics* 666, 48–65. https://doi.org/10.1016/j.tecto.2015.10.014

Vojtko R., Králiková S., Andriessen P., Prokešová R., Minár J. & Jeřábek P. 2017: Geological evolution of the southwestern part of the Veporic Unit (Western Carpathians):based on fission track and morphotectonic data. *Geologica Carpathica* 68, 285–302. https://doi.org/10.1515/geoca-2017-0020

Vozárová A. 1990: Development of metamorphism in the Gemeric/Veporic contact zone (Western Carpathians). *Geologický zborník – Geologica Carpathica* 41, 475–502.

Vozárová A. 1996: Tectono-sedimentary evolution of late Paleozoic basins based on interpretation of lithostratigraphic data (Western Carpathians, Slovakia). *Slovak Geological Magazine* 3–4/96, 251–271.

Vozárová A. & Vozár J. 1988: Late Paleozoic in West Carpathians. *Geol. Inst. D. Štúr*, Bratislava, 1–314.

Vrabec M., Janák M., Froitzheim N. & De Hoog C.J. 2012: Phase relations during peak metamorphism and decompression of the UHP kyanite eclogites, Pohorje Mountains (Eastern Alps, Slovenia). *Lithos* 144, 40–55. https://doi.org/10.1016/j.lithos.2012.04.004

Vrána S. 1964: Chloritoid and kyanite zone of Alpine metamorphism on the boundary of the Gemerides and the Veporides (Slovakia). *Krystalinikum* 2, 125–143.

Vrána S. 1966: Alpidische Metamorphose der Granitoide und Foederata-Serie im Mittelteil der Veporiden. *Sborník geologických vied, Rad ZK* 6, 29–84.

Vrána S. 1980: Newly-formed Alpine garnets in metagranitoids of the Veporides in relation to the structure of the Central zone of the West Carpathians. *Časopis pro mineralogii a geologii* 25, 41–54.

White R.W., Powell R. & Holland T.J.B. 2007: Progress relating to calculation of partial melting equilibria for metapelites. *Journal of Metamorphic Geology* 25, 511–527. https://doi.org/10.1111/j.1525-1314.2007.00711.x

White R.W., Powell R., Holland T.J.B., Johnson T.E. & Green E.C.R. 2014: New mineral activity–composition relations for thermodynamic calculations in metapelitic systems. *Journal of Metamorphic Geology* 32, 261–286. https://doi.org/10.1111/jmg.12071

Wing, B. A., Ferry, J. M. & Harrison, T. M. 2003: Prograde destruction and formation of monazite and allanite during contact and regional metamorphism of pelites: petrology and geochronology. *Contributions to Mineralogy and Petrology*, 145, 228–250.

Xiang H. & Connolly J.A.D. 2021: GeoPS: An interactive visual computing tool for thermodynamic modelling of phase equilibria. *Journal of Metamorphic Geology* 40, 243–255. https://doi.org/10.1111/jmg.12626

Yang P. & Pattison D. 2006: Genesis of monazite and Y zoning in garnet from the Black Hills, South Dakota. *Lithos* 88, 233–253. https://doi.org/10.1016/j.lithos.2005.08.012

Electronic supplementary material is available online:
Supplementary Table S1 at https://geologicacarpathica.com/data/files/supplements/GC-76-Janak_TableS1.xlsx